

## Ages of large lunar impact craters and implications for bombardment during the Moon's middle age

Michelle R. Kirchoff\*, Clark R. Chapman, Simone Marchi, Kristen M. Curtis, Brian Enke, William F. Bottke

Southwest Research Institute, 1050 Walnut Street, Suite 300, Boulder, CO 80302, United States

### ARTICLE INFO

#### Article history:

Received 20 October 2012

Revised 28 February 2013

Accepted 10 March 2013

Available online 1 April 2013

#### Keywords:

Moon, Surface

Cratering

Impact processes

### ABSTRACT

Standard lunar chronologies, based on combining lunar sample radiometric ages with impact crater densities of inferred associated units, have lately been questioned about the robustness of their interpretations of the temporal dependence of the lunar impact flux. In particular, there has been increasing focus on the “middle age” of lunar bombardment, from the end of the Late Heavy Bombardment ( $\sim 3.8$  Ga) until comparatively recent times ( $\sim 1$  Ga). To gain a better understanding of impact flux in this time period, we determined and analyzed the cratering ages of selected terrains on the Moon. We required distinct terrains with random locations and areas large enough to achieve good statistics for the small, superposed crater size–frequency distributions to be compiled. Therefore, we selected 40 lunar craters with diameter  $\sim 90$  km and determined the model ages of their floors by measuring the density of superposed craters using the Lunar Reconnaissance Orbiter Wide Angle Camera mosaic. Absolute model ages were computed using the Model Production Function of Marchi et al. (Marchi, S., Mottola, S., Cremonese, G., Massironi, M., Martellato, E. [2009]. *Astron. J.* 137, 4936–4948). We find that a majority (36 of 40) of our superposed crater size–frequency distributions are consistent with the Model Production Function. A histogram of the original crater floor model ages indicates the bombardment rate decreased gradually from  $\sim 3.8$  Ga until  $\sim 3.0$  Ga, implying an extended tail to the Late Heavy Bombardment. For large craters, it also preliminarily suggests that between  $\sim 3.0$  and  $1.0$  Ga bombardment may be characterized by long periods ( $>600$  Myr) of relatively few impacts (“lulls”) broken by a short duration ( $\sim 200$  Myr) of relatively more impacts (“spike”). While measuring superposed craters, we also noted if they were part of a cluster or chain (named “obvious secondary”), and analyzed these craters separately. Interestingly, we observe a wide variety of slopes to the differential size–frequency power-law, which demonstrates that there can be considerable variation in individual secondary crater field size–frequency distributions. Finally, four of the small, superposed crater size–frequency distributions are found to be inconsistent with the Model Production Function; possible reasons are: resurfacing has modified these distributions, unrecognized secondary craters, and/or the Model Production Function has incorrect inputs (such as the scaling law for the target terrain). The degraded appearance of the superposed craters and indications of resurfacing suggest that the first cause is the most likely.

© 2013 Elsevier Inc. All rights reserved.

### 1. Introduction

Standard lunar chronologies (Hartmann et al., 1981; Neukum et al., 2001; Stöffler and Ryder, 2001) have been based on combining lunar sample radiometric ages with inferred impact crater densities of features or geological units from which the samples have been interpreted to come. In particular, there has been increasing focus on terrestrial planetary cratering from the declining phases of the Late Heavy Bombardment (LHB,  $\sim 4$  Ga; see Table 1 for summary of all acronyms) through the middle of planetary history ( $\sim 1$  Ga). Lately, however, there has been increasing skepticism that

these interpretations of how the impact flux on the Moon has changed with time during this “middle age” of bombardment are robust. There are three critical elements in deriving the lunar impact chronology: the association of the samples with the units on which superposed craters are counted, the measurements of relative crater density, and the sample ages themselves.

First, the Apollo-era lunar sample investigators, and the more recent evaluations and syntheses of that work (Stöffler and Ryder, 2001; Wilhelms, 1987), put together the best sample and terrain associations they could with the available data. But many uncertainties remain or have even arisen as a result of the recently renewed interest in the Moon and data from several lunar spacecraft in the past decade. For example, the earlier assignments of Apollo sample ages to specific basins have been increasingly

\* Corresponding author. Fax: +1 303 546 9687.

E-mail address: [kirchoff@boulder.swri.edu](mailto:kirchoff@boulder.swri.edu) (M.R. Kirchoff).

**Table 1**  
Summary of acronyms used in text in the order they appear.

Acronym	Description
LHB	Late Heavy Bombardment
LROC	Lunar Reconnaissance Orbiter Cameras
MBA	Main belt asteroid
SFD	Size–frequency distribution
NEO	Near Earth Object
SSC	Small, superposed crater
WAC	Wide Angle Camera
OS	Obvious secondary
CF	Crater floor
MPF	Model Production Function
NAC	Narrow Angle Camera
USGS	United States Geological Survey

questioned, in part based on new imaging of the Moon by the Lunar Reconnaissance Orbiter Camera (LROC). The age of Nectaris has long been disputed, but the once accepted age of Serenitatis is now also seriously challenged by interpretations of new images of the Serenitatis region (Spudis et al., 2011). Post-LHB ages are often based on assumptions that the samples are from the sampling localities rather than being ejecta from some distant locations. Alternatively, ages for some distant features (e.g., Copernicus, which is not near an Apollo or Luna site) were derived assuming that they are *not* local samples but are indeed ejecta from the distant feature, based on circumstantial evidence like a ray crossing the locality.

Second, the crater measurements are also problematical. Ideally, one wants to have a good statistical count of superposed craters on a homogeneous geological unit. But for various reasons (one being the small size of many units, hence a preference to use an age-dating method using the much more numerous small craters), much of the early post-Apollo crater age dating was based on the  $D_L$  criterion, which is an estimated diameter ( $D$ ) for craters degraded to nearly the point of invisibility by smaller superposed craters (Boyce and Dial, 1975; Soderblom and Lebofsky, 1972). This now abandoned method invoked a fairly simplistic theoretical model for crater degradation by saturation cratering in a regolith. Discrepancies are fairly common between results of this technique compared with newer, presumably better, techniques (see discussions by Hiesinger et al. (2000, 2010)).

The third element of the crater chronology technique, the sample ages, have minor issues of methodological uncertainties (e.g., Stöffler and Ryder, 2001 and references therein), including overall calibration issues. However, these seem to be less serious than problems with the other two elements – the crater statistics and the associations between the samples and the units studied for crater density.

The LHB and the shape of the impact flux curve for the Moon during ensuing eons has become a matter of much current interest for several reasons. First, there has been a re-examination of the LHB itself (cf. review by Chapman et al. (2007)), with a few investigators continuing to doubt that a “narrow spike” LHB or “terminal cataclysm” occurred at all (Hartmann, 2003; Neukum and Ivanov, 1994). More recently, Morbidelli et al. (2012) have proposed a “saw-tooth” LHB with a wider “spike” and overall lower bombardment rates. This has been hypothesized in the context of a theoretical model for an early extension of the main belt asteroid (MBA) population (the “E-belt”) inward to 1.7 AU from the current inner edge of the belt (Bottke et al., 2012) and new crater measurements of Pre-Nectarian terrains (Marchi et al., 2012). Focusing more on the end of the LHB, there has been a re-examination of what had been traditionally viewed as a change-over in the crater size–frequency distribution (SFD) characteristic of the LHB (what Strom et al. (2005) termed “Population 1”) to the post-LHB bombardment by

“Population 2” crater SFDs due to the currently observable population of near-Earth Objects (NEOs) (Strom et al., 2005; implications have recently been debated by Čuk et al. (2010, 2011) and Malhotra and Strom (2011)). In addition, Fassett et al. (2012) have argued that the shape of the crater SFD changed mid-way through the Nectarian rather than at the end of the LHB, calling into question the origin of impactors during the later stages of the LHB. Finally, other researchers have been trying to assess evidence from other various sources (e.g., ancient terrestrial spherule beds [e.g., Simonson and Glass, 2004]) to establish the bombardment rate on Earth, Mercury, and other bodies during the 2–3 Gyr following the LHB (cf. Bottke et al., 2012).

There are widespread implications for understanding the impact flux curve in the inner Solar System during this middle age. If there are substantial departures from lunar chronologies like the smooth curves of Neukum and Ivanov (1994), Marchi et al. (2009), and Le Feuvre and Wieczorek (2011) then they might correlate with recognizable episodes or durations in the Earth’s geological history. Furthermore, a better understanding of the lunar chronology, as translated to Mercury via dynamical and crater-scaling considerations, might better constrain the possibly very young ages of some volcanic features on Mercury (Marchi et al., 2011; Prockter et al., 2010). There are many other consequences for planetary science, as the Moon is our best witness plate for recording the ancient bombardment by asteroids and comets in the inner Solar System.

In this work, we investigated the ages of distinct features on the Moon that were formed during this period from the ending stages of the LHB toward the present. We employed a methodology introduced by Baldwin (1985), which addressed essentially the same issues still considered today: what was the bombardment rate on the Moon in its middle age. Although his results have substantial statistical uncertainties and were based on the inferior 1960s Lunar Orbiter IV photographs, Baldwin concluded that the impact rate fell to a minimum about 3.1 Ga, and had a fairly abrupt increase in the last 0.3–0.4 Gyr to about double the rate at 3.1 Ga. Other studies have yielded similar, or occasionally discordant, results, but have been based on phenomena that may not be recording impacts by projectiles of sizes that make the craters Baldwin counted (e.g., Culler et al. (2000) studied impact spherules, McEwen et al. (1997) studied farside rayed craters, and Cohen et al. (2005) studied impact melts).

As detailed below, we have a sample of 40 craters of roughly 90 km diameter, ranging from young to old, and we measured the population of small, superposed craters (hereafter also “SSCs”) on their floors. This approach is different from those used previously or currently in the following ways. For our measurements we used the LROC Wide Angle Camera (WAC) mosaic, which is much superior to the Lunar Orbiter images others have employed in the past (e.g., better coverage in both space and pixel scale – especially of the farside, more uniform incidence angle, and reduced image artifacts). Furthermore, we avoided measuring craters on large crater walls, rims, and ejecta blankets, commonly included by others (Baldwin, 1985; Hiesinger et al., 2012). Despite the fact that these are plausibly portions of the original crater, they have sloping crater walls or hilly terrains, which are not valid sampling areas, at least for small craters, because of visibility issues (due to atypical and bad lighting geometry) and mass-wasting problems (which may be greatly enhanced on slopes, thus freshening the surface by a process not active on flat terrains). Furthermore, ejecta blankets are not necessarily solid materials (so scaling relations may differ from those pertaining to most surfaces), rough at the scales of small craters (making identification difficult), and susceptible to older craters “showing through” (leading to spurious ages). Finally, we segregated SSCs formed in clusters and chains (“obvious secondaries”; hereafter also “OSs”) from the others

ultimately used to analyze the crater floors (hereafter also “CFs”), as they are very likely secondary craters.

As we will describe, we have found a number of issues associated with this methodology. Inevitably, especially for younger craters, we have issues of small counting statistics. Although Baldwin recognized the issue of increased numbers of secondary craters among the smaller superposed craters he counted, we found secondaries to be even more problematic, and did our best to separate primaries from secondaries. Our end product for each of the  $D \sim 90$  km craters are SFDs for the SSCs (not only totals but also for OSs and for craters classified by degradational state). To these, we generally applied the Marchi et al. (2009) Model Production Function (hereafter also MPF), which assumes an exponentially decreasing ( $\geq 3.5$  Ga), then constant flux ( $\lesssim 3.5$  Ga) for small ( $D \sim 1$  km) craters, to calculate model ages for the floors. We note that many of the CFs are evidently not the original floors but have been subsequently modified, e.g., by volcanic flooding, ejecta deposits from other craters, and/or mass-wasting of the crater’s interior walls. In the end we have, subject to numerous caveats, a histogram of ages for the lunar terrains analyzed.

## 2. Methods

### 2.1. Selection of crater floors

For this study, we required well-defined terrains with different ages and random locations on the lunar surface, ideally with areas large enough to achieve good statistics for the SSC ( $D \approx 0.6$ – $15$  km) SFDs to be compiled. Therefore, we selected the floors of larger impact craters, which best combine these characteristics. Most of the selected large craters (38 of 40) have  $D = 80$ – $100$  km (Fig. 1, Table 2). These 38 CFs were chosen from an initial database of 151 named craters with  $D = 80$ – $100$  km available through the IAU Gazetteer of Planetary Nomenclature (<http://planetary-names.wr.usgs.gov/Page/MOON/target>). Two additional selections, Al-Biruni ( $D = 76$  km,  $18^\circ\text{N}$ ,  $93^\circ\text{E}$ , #27 in Fig. 1, Table 2) and Hausen ( $D = 163$  km,  $65^\circ\text{S}$ ,  $88^\circ\text{W}$ , #13), were included because they met most our criteria, after being examined for separate, unrelated tasks.

Four criteria were used to reduce the 151 named craters down to the random sample of 38 that we ultimately used (so our project could be completed in a reasonable time frame). The first criterion

encompassed all aspects of the quality of CF image coverage requisite for identifying and measuring SSCs. The image basemap chosen for this work was the global LROC WAC 100 m/pixel mosaic (<http://www.lroc.asu.edu/>, Robinson et al., 2010). We foremost required image coverage at reasonably low lighting angle (i.e., solar incidence angle between  $\sim 60^\circ$  and  $80^\circ$ ). Thereafter, we avoided mosaic seams that mix opposing lighting directions or that do not spatially correspond well, distorted images, and small missing image sections. This first criterion removed  $\sim 23\%$  from the initial list of 151 craters.

The second criterion avoided high densities of secondary craters to obtain reliable SSC SFDs for analyses. Secondary craters are produced by debris expelled from large primary impacts, not by external impactors, and form all at once relative to the geologic timescale (e.g., McEwen and Bierhaus, 2006; Melosh, 1989). Therefore, because our goals were to compute the ages of the CFs and study the evolution of the sources of the impactors that produce the SSCs, inclusion of secondary craters should be minimized as much as possible. However, some CFs have so many superposed OSs (craters forming prominent clusters or chains) that it becomes questionable that a significant number of the SSCs not recognized as OSs are primaries. This follows from the fact that not all secondaries form in clusters or chains, and the probability of isolated secondaries increases around already recognized clusters and chains (e.g., McEwen and Bierhaus, 2006). Accordingly, our criterion was to exclude CFs with SSC distributions composed of mostly OSs, which was determined qualitatively by the observer. This removed another  $\sim 19\%$  from the initial list of 151 craters.

The third criterion was the ability to define adequate SSCs measurement areas. Identifiable crater floors were the primary requisite, which in general requires that the crater rim is mostly intact. Furthermore, we sought to acquire measurement areas large enough to get a good statistical representation of the SSC SFDs. Areas of at least  $1000$  km<sup>2</sup> were found to be adequate (depending on terrain age). However, this was not always achievable, since we required that the measurement area included only one coherent geologic unit, and some resulting areas were smaller than ideal (areas for each CF are given in a summary file and in each “read me” file in the Supplementary material). These craters are noted in the results below. Nevertheless, CFs were excluded that had final measurement areas of  $<600$  km<sup>2</sup> after removing units, such as ejecta blankets, wall collapses, and tectonic features, emplaced after

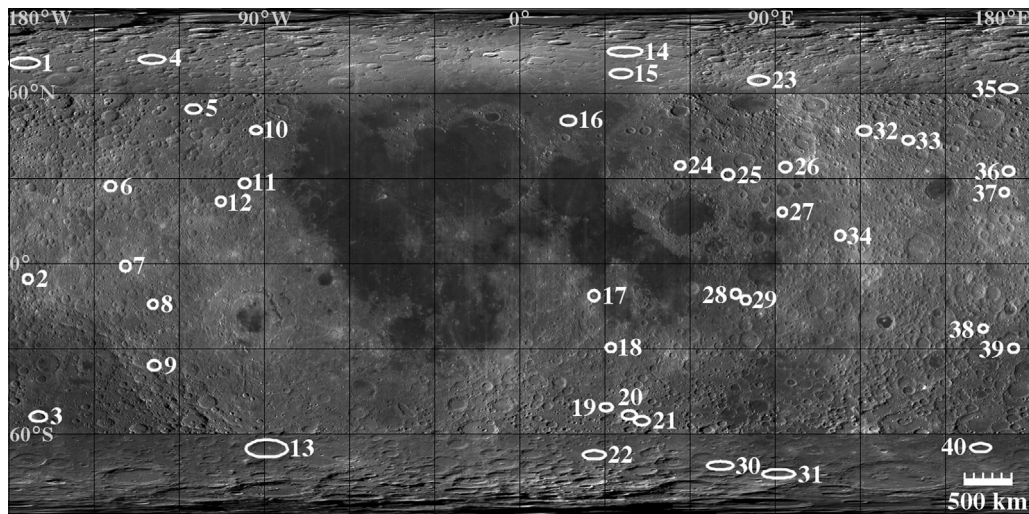


**Fig. 1.** Locations of the CFs we analyze in this work are marked by white circles (stretched away from equator due to projection). Numbers correspond to the numbers in Table 2. Background is LROC WAC 100 m/pixel mosaic (<http://www.lroc.asu.edu/>, Robinson et al., 2010) projected in simple cylindrical format and scale at the equator is indicated.

**Table 2**  
List of large craters studied.

# <sup>a</sup>	Crater name	D, km	Center lat., lon.	# <sup>a</sup>	Crater name	D, km	Center lat., lon.
1	Roberts	89	71°N, 174°W	21	Rosenberger	92	56°S, 43°E
2	Icarus	94	6°S, 173°W	22	Manzinus	98	68°S, 26°E
3	Bose	95	54°S, 169°W	23	Hayn	86	64°N, 84°E
4	Mezentsev	85	72°N, 130°W	24	Geminus	83	34°N, 57°E
5	Coulomb	90	54°N, 115°W	25	Hahn	88	31°N, 74°E
6	Joule	98	27°N, 144°W	26	Vestine	98	34°N, 94°E
7	Vavilov	99	1°S, 139°W	27	Al-Biruni	76	18°N, 93°E
8	Ioffe	84	14°S, 129°W	28	La Pérouse	80	11°S, 76°E
9	Langmuir	92	36°S, 129°W	29	Ansgarius	95	13°S, 80°E
10	McLaughlin	80	47°N, 93°W	30	Neumayer	80	71°S, 71°E
11	Laue	89	28°N, 97°W	31	Hale	84	74°S, 92°E
12	Robertson	90	22°N, 105°W	32	Millikan	96	47°N, 121°E
13	Hausen	163	65°S, 88°W	33	Bridgman	82	43°N, 137°E
14	Baillaud	89	75°N, 37°E	34	Lobachevskiy	88	10°N, 113°E
15	Arnold	93	67°N, 36°E	35	Tikhov	86	62°N, 172°E
16	Aristoteles	88	50°N, 17°E	36	Shayn	93	33°N, 172°E
17	Theophilus	99	12°S, 26°E	37	Freundlich	85	25°N, 171°E
18	Piccolomini	88	30°S, 32°E	38	Paracelsus	82	23°S, 164°E
19	Pitiscus	82	51°S, 31°E	39	Birkeland	84	30°S, 174°E
20	Vlacq	91	54°S, 39°E	40	Lyman	83	65°S, 163°E

Crater data from <http://planetarynames.wr.usgs.gov/Page/MOON/target>.

<sup>a</sup> Corresponds to number in Fig. 1.

the primary geologic unit (e.g., original crater floor or mare expanse). This removed another 32% from the initial list of 151 craters.

The fourth criterion was that we observe at least 10 SSCs with  $D > 600$  m in order to be able to adequately analyze their SFDs with the techniques described below. This prohibited analyzing the youngest craters, such as Tycho and Copernicus, because they have only a few SSCs in our size range. Previous determinations of these craters' ages have commonly used smaller superposed craters ( $D \leq 100$  m), with the most recent efforts using LROC Narrow Angle Camera (NAC) images (pixel scale of 0.5–2 m/pixel) (e.g., Hartmann et al., 1981; Hiesinger et al., 2012; Neukum and Ivanov, 1994). Such small craters are generally below the resolution of the mosaic we used and may be secondary rather than primary craters. Removal of Tycho and Copernicus is a tiny change to our sample size, resulting in the final catalog of 38 craters used for this study (Fig. 1, Table 2).

These criteria to reduce the dataset size have produced a bias against the youngest and oldest CF ages for our final dataset. We estimate that we cannot compute the ages of mid-sized CFs that are younger than  $\sim 1$  Ga with our SSC diameter range. Therefore, we cannot make any conclusions about trends in impact rate younger than this. The database also lacks very old CFs ( $\geq 4$  Ga), which is generally a result of excluding CFs with many OSs and heavily degraded surfaces. However, there are possible further limitations for studying very old lunar terrains. First, resurfacing during the LHB and later epochs may have eliminated very old relatively flat terrains of considerable size (e.g., at least a few hundred km<sup>2</sup>), needed to measure SSCs. Second, there may be wide-spread obliteration of old ( $>4$  Ga) small craters by substantial degradation (Craddock and Howard, 2000). However, our goal was to study bombardment for the interval younger than  $\sim 4$  Ga, so these limitations are inconsequential to this work. Otherwise, we do not believe these criteria bias age in the range between  $\sim 4$  and 1 Ga, and we probably have a random sample of ages.

We note that there is a lack of CFs analyzed on the lunar near-side maria (Fig. 1). This is for two reasons. One, larger craters ( $D = 80$ –100 km) older than the maria have likely been completely erased. Two, larger craters ( $D \geq 80$  km) younger than the maria are rare. Maria are relatively young surfaces on the Moon, and the production of large craters after their formation was declining rapidly.

Furthermore, one of them, Copernicus, is so young that it had to be excluded for that reason (inadequate statistics as discussed above).

## 2.2. Measurement of small, superposed craters

For each CF in the database, we first drew the boundaries outlining portions of the floor within which the SSCs are measured. As mentioned above, our most important condition for the boundary position and measurement area was to include only one geological unit. However, sometimes borders between geological units (e.g., floor and thin superposed ejecta or collapse feature, or two mare flows) are so subtle that they were hard to distinguish. Thus, while obvious deviations were excluded, we cannot guarantee that each boundary contains only one unit. However, units with such similar characteristics are not likely to be extremely different in age. As a secondary check we mapped our final crater measurements (e.g., Fig. 3a) to look for very obvious changes in crater density within the boundary, and altered the boundary to exclude any regions that showed extensive differences. We also used the United States Geological Survey (USGS) Geologic Atlas of the Moon produced in the 1960s and 1970s to assist in interpreting geological units (nicely organized at <http://www.lpi.usra.edu/resources/mapcatalog/usgs/>). Primarily the 1:5,000,000 lunar hemispheric maps were used, except for a few nearside craters that were mapped in the 1:1,000,000 series. Finally, if the CF was resurfaced, large craters were occasionally observed to not be on top of the geological unit being measured, but appeared to be partially resurfaced by the same event. Therefore, these craters were considered to not be superposed on the geological unit of study and were not measured.

The other important consideration in choosing the measurement area was to avoid substantially large central peaks and crater walls, because their sloped surfaces and resulting mass-wasting tend to increase the rate of removal of small craters that form there. Some counting areas did include small central peaks, which does not constitute a large portion of the counting area as qualitatively determined by the observer, and thus did not greatly affect the final SSC SFD statistics. Fig. 2 illustrates two example counting areas for Vavilov and Piccolomini CFs (the rest are shown in the Supplementary material).

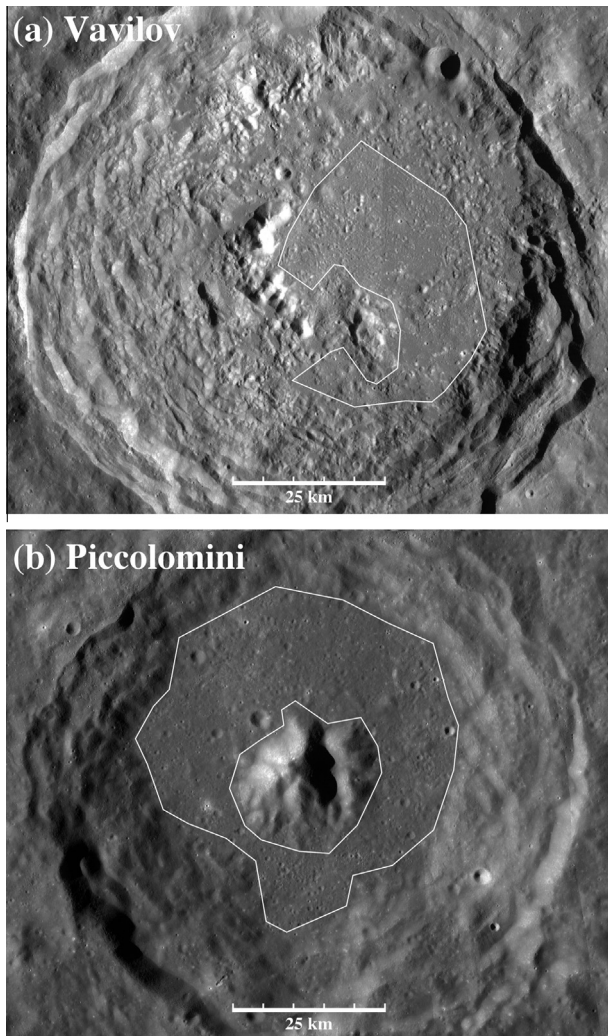


**Fig. 2.** (a) Vavilov crater ( $D = 99$  km,  $1^{\circ}\text{S}$ ,  $139^{\circ}\text{W}$ ). (b) Piccolomini crater ( $D = 88$  km,  $30^{\circ}\text{S}$ ,  $32^{\circ}\text{E}$ ). These are two examples of counting area outlines (white) selected for CFs. SSCs are measured within these areas. In (a) the left side of the crater floor is avoided because it appears to be covered by a subsequent wall collapse. In (b) the large central peak is excluded, along with two regions in the south that are likely wall collapses. North is up in both images and scale is indicated.

All of the recognizable SSCs within the defined boundaries were measured. In compiling the SSC crater databases, the first step was to identify which features are impact craters and not some other geological feature, such as grooves or pits. This is especially a challenge on CFs that are hummocky (Vavilov is a good example, Fig. 2). After the identification of a SSC was accepted, then the rim-to-rim diameter was measured using the 3-point crater tool in JMARS for the Moon (<http://www.jmars.asu.edu/>). This tool calculates the best-fit circle to three points chosen around the SSC rim. For elliptical craters, we consistently chose points such that the circle diameter corresponded to the long axis. For a few of the CFs (Neumayer, Bridgman, and Icarus), an automated technique (Burl et al., 2001) was used to initially identify and measure SSCs. The automated output was always inspected and corrected by at least one of us for false positive identifications (removed), missed identifications (added), and erroneous measurements (manually adjusted to better fit the crater rim).

The next step was to classify measured SSCs. First, we determined if any identified SSCs are OSs. OSs were identified based solely upon qualitatively observed spatial morphology, i.e., if they occur in a cluster or chain as recognized by the human observer.

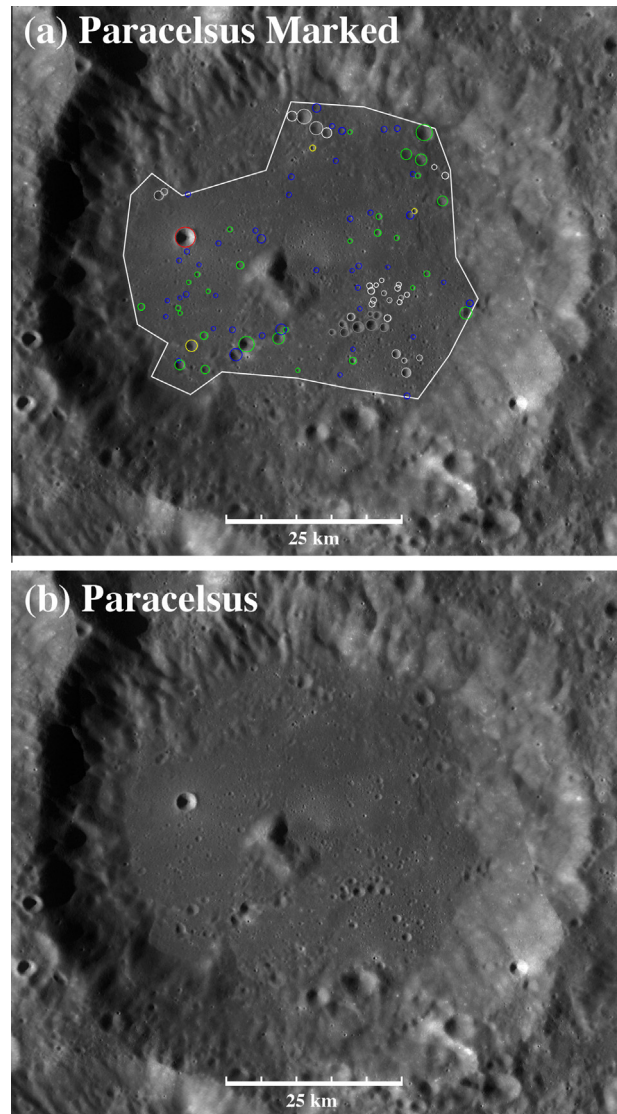


**Fig. 3.** Paracelsus crater ( $D = 82$  km,  $23^{\circ}\text{S}$ ,  $164^{\circ}\text{E}$ ). (a) Identified and classified SSCs on the CF. Colored circles designate probable primary craters of degradation class 4 (blue), class 3 (green), class 2 (yellow), and class 1 (red). White and gray circles designate OSs of degradation class 4 (white), class 3 (light gray), class 2 (medium gray). (b) Same image without markings for comparison. North is up in both images and scale is indicated.

An example is shown in Fig. 3, where OSs are marked by white or gray circles. Then each crater was assigned a degradation class on a scale of 1–4. This straightforward scale is derived from the one used many decades ago to generate the Lunar and Planetary Laboratory lunar crater database (Arthur et al., 1963), and has been widely applied in planetary cratering studies since then. Class 1 signifies the freshest craters with sharp rims and deep bowls. Class 2 is the next freshest, with slight degradation of the rim and infill of the bowl. Class 3 craters have even more degraded rims (possibly even partially missing), and are appreciably shallower. Lastly, the most shallow, degraded craters with little to no rims, are designated class 4. Examples of these are shown in Fig. 4 and example SSC identifications in our work are shown in Fig. 3. The pixel scale of the WAC mosaic of 100 m/pixel and average size of the areas counted typically limited the size range of the SSCs identified to between  $D \sim 600$  m (resolution limit) to 15 km (largest crater measured). Finally, in subsequent figures and discussion, the measured

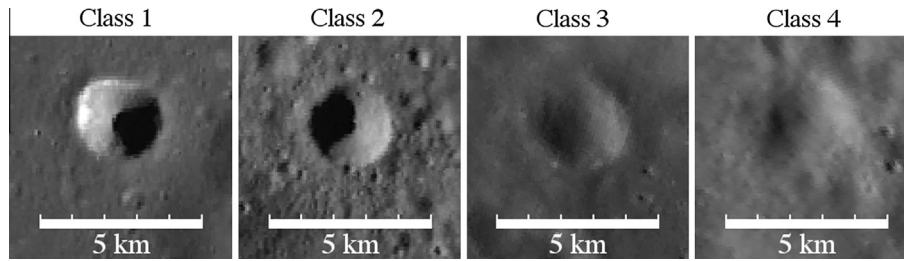


**Fig. 4.** Model examples for lunar simple craters of the degradation classes we use in this work. Derived from the classifications initialized by the Lunar and Planetary Laboratory lunar crater catalog (Arthur et al., 1963). Degradation increases to the right. Images are from the LROC WAC mosaic and scale is indicated.

**Table 3**  
Example of binning for Paracelsus crater floor.

Bin #	Bin size	# Of craters
1	0.63–0.83	38
2	0.83–1.08	19
3	1.08–1.62	9
4	1.62–2.43	7
5	2.43–3.65	2

SSC SFDs presented are all of these degradation classes combined, but excluding OSs, unless otherwise noted.

### 2.3. Analysis of small, superposed crater size–frequency distributions

After the SSC databases were completed, we used several techniques to analyze them. One was to compute the differential slope,  $b$  (in  $\frac{dN_{cum}}{dD} \propto D^b$ , where  $N_{cum}$  is the cumulative density of craters with  $D \geq$  given diameter) for each SSC SFD (Tables 4–6). Diameters were binned between two values ( $D_1$ ,  $D_2$ ) using a more flexible technique than the traditional square-root-two binning (Crater Analysis Techniques Working Group, 1979). To start,  $D_1$  of the first bin was set to be the resolution cut-off diameter, which is the smallest diameter before the crater density begins to sharply decrease (“roll-off diameter”). The  $D_2$  value was then selected so that the number of SSCs in that bin is about half of the total number of SSCs in the database. Subsequent bins were then chosen to have very roughly half of the number of SSCs in the previous bin. For the last bin, the diameter range was specified so that the median value for the bin was more or less the largest crater diameter observed for that SSC distribution. An example for SSCs within Paracelsus is provided in Table 3. Our technique prevented bins with zero craters from falling in-between bins with craters and it reduced the number of bins with only one crater, by increasing bin size for larger diameters. After the SSC SFD was appropriately binned, a Gauss–Newton based non-linear least squares fitting routine in the statistical package *R* (<http://www.r-project.org/>) was used to compute  $b$  for each crater SFD. This routine does use the errors on each data point ( $\sqrt{n_{bin}/area}$ , where  $n_{bin}$  is the number of SSCs in each bin) as weights in the fit to reduce  $\chi_2$ . The outputs are the best-fit slope and the  $1\sigma$  error. Outputs for each fit are given in the Supplementary material.

Another technique utilized was plotting in log–log space the SSC SFDs (crater density vs.  $D$ ) in relative (*R*) plot format (e.g., Fig. 10, [Crater Analysis Techniques Working Group, 1979]). The *R*-plot normalizes the differential crater SFD by dividing by one with a differential slope,  $b = -3$  in order to emphasize small changes in the crater SFD slope with diameter. This type of plot is well suited for comparing crater SFDs from different terrains to understand if they have similar or different characteristics. The same diameter bin sizes from the differential slope calculation were used for each crater SFD. Error bars on each data point are again  $\sqrt{n_{bin}/area}$ .

### 2.4. Crater floor model ages

Lastly, we determined relative crater densities and absolute model ages of the CFs examined. Relative crater densities are straightforwardly the observed cumulative density of SSCs at  $D = 1$  km along with the  $\sqrt{N_{cum}/area}$  error. These values can be directly input into other production functions and chronologies to obtain absolute model ages (although a fit to the full cumulative crater SFD like we used here would be best), or on their own as an indication of finer scale differences in relative stratigraphy. Our absolute model ages were computed by fitting our entire SSC cumulative SFDs with the MPF of Marchi et al. (2009). The MPF used for this work is produced by using impact crater scaling laws to convert observations and collisional evolution models of NEOs to crater SFDs. A variety of scaling laws are possible that depend on the physical assumptions used for the cratering process. Our calculations used the Pi-scaling law for the gravity regime (Schmidt and Housen, 1987) as given by the formulation of Melosh (1989, p. 118–119). This was a logical one to start with as our measured SSCs are larger than the estimated strength-to-gravity transition diameter of a few hundred meters for the Moon (Melosh, 1989, p. 120). We will discuss in Section 4 the effects of using other scaling laws, especially those that include the strength regime, on the MPF and fits to our small, SSC SFDs.

The MPF was fit to the SSC cumulative SFDs to determine the production function density at  $D = 1$  km. The best fit was determined by minimizing  $\chi^2$ , where each cumulative density value was weighted by its associated  $\sqrt{N_{cum}/area}$  error. Note that the purely statistical  $\sqrt{N_{cum}}$  errors reported are minimum values. Actual errors are larger because of systematic errors associated with human recognition of impact craters, subjectiveness of locating the resolution roll-off diameter, and the finite area of the regions analyzed. The first influences all diameters, while the second is important for only small diameters, and the third is important for only the largest SSCs measured here ( $D \geq 3$  km), which have sizes that approach a significant fraction of the regions analyzed. However, all of these systematic errors are difficult to quantify without many repetitions of the measurements, and are not reported.

To determine if the “best fit” actually demonstrates good agreement between the data and the MPF, we evaluated qualitatively how many data points matched the model MPF, especially considering the error. If most (>80%) of the points fell along the line, then the crater SFD is fit well by the MPF. If several ( $\geq 3$ ) points in a row did not fall along the MPF, this did not necessarily indicate a poor fit, but required further investigation. This is a principal consequence of a characteristic of the cumulative representation of the crater SFD such that each data point incorporates the previous ones going from large to small diameters. For example, if the largest crater(s) measured in the area is removed from the SSCs, the crater SFD very likely obtains a new slope, which may or may not be more consistent with the MPF. Therefore, the largest craters have disproportional

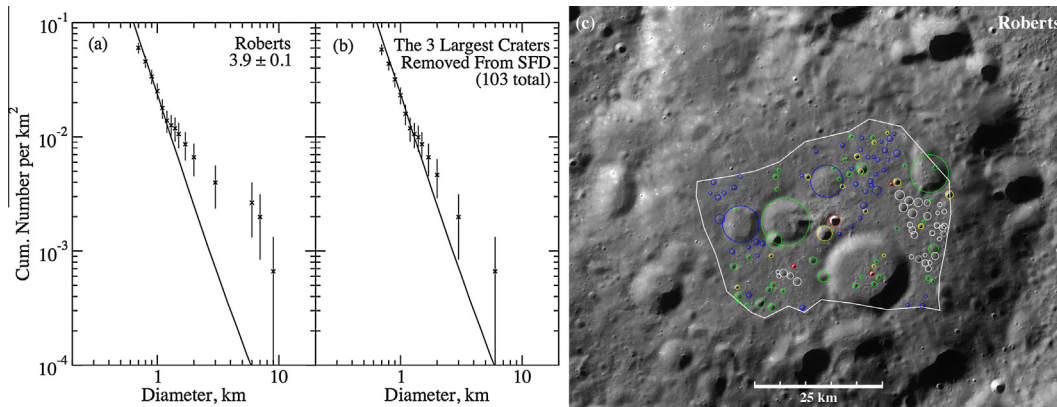


**Fig. 5.** Illustration of our analysis to determine if there is good agreement between the “best fit” MPF and a SSC SFD that has several data points significantly away from the MPF using Roberts crater ( $D = 89$  km,  $71^\circ\text{N}$ ,  $174^\circ\text{W}$ ). (a) Full crater SFD (x’s; represents all colored circles in (c), excluding the white and gray circles, which are OSs) compared with the “best fit” MPF (solid line). About 6 data points for  $D > 2$  km fall significantly away from the line. (b) Modified crater SFD with the 3 largest craters removed. The remaining data points for  $D > 2$  km fall much closer to the line indicating good agreement between the MPF and the SSC SFD. This occurs because each data point incorporates the previous from large to small craters when the crater SFD is computed in cumulative format. Therefore, the largest diameter bins, which are the most uncertain, have undue influence on the shape of the crater SFD. (c) SSCs measured on Roberts CF. North is up and scale is indicated. The largest crater was not measured per our measurement criteria of one geological unit defined in Section 2.2; we propose that it was formed before the resurfacing event that produced the current CF, and is thus not a superposed crater.

influence on the shape of the crater SFDs, as the largest craters have the poorest statistics and are not well represented within these small study areas (see below). Consequently, apparent divergent trends of the data from the MPF may not be statistically significant. For nine of our SSC SFDs, we observed that three or more of our largest crater diameter bins had a higher density (shallower cumulative slope with increasing diameter) than was expected by the MPF, and fell above the MPF in a cumulative plot (e.g., Fig. 5). To ascertain if these apparent divergent trends above the MPF observed in our data could be real, we removed the largest craters from each pertinent SSC SFD (e.g., Fig. 5). If only a small number (2 or 3) of the large craters needed to be removed to obtain a better fit with the MPF, then the original fit including the large craters is considered good (Roberts [Fig. 5], Bose, Tikhov, Laue, Freundlich). If a considerable number of large craters ( $\geq 4$ ) had to be removed to get a better fit, then the original fit is considered poor (Rosenberger, Mezentssev, Millikan, and Shayn). Note that we did not observe any divergent trends with large crater diameter bins with lower density (steeper cumulative slope) and falling below the MPF in our data. This observation will be discussed further in Section 4.2.

Using these qualifications, we found that a majority of the SSC SFDs are fit well by the MPF (Table 4, Fig. 6). This could be viewed as a surprise, considering the different formation epochs of the superposed craters and the probable changes that have taken place in the primary source regions of lunar impactors. To zeroth order, one might instead expect to see more dramatic changes in the impactor SFD over time. For example, consider that if the inner and central asteroid belt produces most lunar impactors over time, as predicted by dynamical models (Bottke et al., 2002, 2006a), major family-forming events there could potentially modify what ends up hitting the Moon over some extended interval of time.

On the other hand, a lack of change actually matches expectations obtained from main belt collisional and dynamical evolution models. Numerical work shows that collisional evolution reshapes the main belt size distribution into a characteristic wavy shape with inflection points near  $D \sim 0.001$  m, 0.1 km, a few km, and 100 km (Bottke et al., 2005a, 2005b). The shape and absolute number of objects in this impactor SFD has been shown to be remarkably constant over billions of years of simulation time for small asteroids sizes (i.e., variation of less than factor of 2 over the last 3.5 Gyr; Bottke et al., 2005b). Major family-forming events can and do produce sudden perturbations to this population, but most

lack sufficient mass to “beat the background” and change the shape of the impactor SFD for very long (Bottke et al., 2005a; Farley et al., 2006). Collisional evolution is particularly efficient at grinding up small asteroids because catastrophic disruption laws show a transition from the strength- to gravity-scaling regimes near  $\sim 100$  m (Asphaug et al., 2002). Marchi et al. (2013) argued this modeling work probably explains why small craters on Vesta’s non-saturated terrains (within or near the Marcia crater and Rheasilvia basin), as well as those found on (951) Gaspra, all have a crater SFD with the same shape.

Keeping this in mind, one must also consider that most of the small asteroids striking the Moon escaped the main belt through a combination of Yarkovsky thermal forces, which give small asteroids mobility in semimajor axis, and resonances (Bottke et al., 2006b). Thus, for small objects, one could consider the lunar impactor population to be a tiny subset of the main belt SFD (with some minor differences; see Morbidelli and Vokrouhlický, 2003) that happens to reside on Earth/Moon-crossing orbits, with the steady state population on the order of 1/1000th of the main belt population. Thus, if the flux of small bodies out of the main belt is substantial enough that it is essentially always dominated by background main belt objects, the superposed craters examined here could easily keep the same shape for, say, the last 3.5 Gyr. Moreover, short term perturbations to the impact flux may also be hard to detect in many crater records because the signal produced has to beat out the background crater population. For our data, the cumulative density value at  $D = 1$  km derived from the fit to the full SSC SFD was then used to get the absolute model age using the calibrations from previous crater counts on regions with possibly associated radiometric ages (Marchi et al., 2009; Stöffler and Ryder, 2001). The chronology used here assumed the flux for the impactors that formed the SSCs we observe decayed exponentially from  $\sim 4.5$  to 3.5 Ga, then was constant from  $\sim 3.5$  Ga to present.

We agree that the derived lunar chronologies used to date likely have their issues (as discussed in the Introduction). All are based on limited data and possibly problematic assumptions. For the former, consider that very few lunar terrains with superposed small craters have calibrated ages from lunar samples (e.g., we are limited to a few very young lunar craters, small terrains near the  $\sim 0.11$  Ga Tycho crater, the  $\sim 0.8$  Ga Copernicus crater, and some broader mare terrains that date back to 3.2 Ga and older). For the latter, it is often assumed that the lunar impact flux for small

**Table 4**  
Small, superposed crater size–frequency distributions that are consistent with Model Production Function.

Crater name <sup>a</sup>	Model age <sup>b</sup>	Stöffler epoch <sup>c</sup>	USGS epoch <sup>d</sup>	Relative crater density <sup>e</sup>	$b^f$	$D$ range	Original floor <sup>g</sup>
Vavilov, 7	1.7 ± 0.1*	Eratos.	Coper.	2400 ± 1700	−5.8 ± 1.2	0.6–1.2	Likely
Hayn, 23	1.8 ± 0.4*	Eratos.	Coper.	2100 ± 1200	−4.5 ± 1.3	0.6–1.1	Likely
Aristoteles, 16	2.7 ± 0.8*	Eratos.	Eratos.	1600 ± 1200	−5.9 ± 1.1	0.6–1.2	Possibly
Theophilus, 17	3.0 ± 0.6*	Eratos.	Coper.†	6100 ± 2200	−4.7 ± 1.0	0.6–1.2	Likely
Geminus, 24	3.2 ± 0.4*	Er./Im.	Eratos.	3000 ± 1800	−5.4 ± 1.8	0.7–1.2	Likely
Hale, 31	3.3 ± 0.2*	L. Imb.	L. Imb.	4500 ± 2700	−3.8 ± 1.0	0.7–1.5	Likely
Langmuir, 9	3.5 ± 0.1*	L. Imb.	Imbr.	4600 ± 2700	−4.7 ± 1.0	0.7–1.4	Not likely
Lyman, 40	3.5 ± 0.1	L. Imb.	L. Imb.	4900 ± 1900	−4.4 ± 0.8	0.7–1.7	Likely
Hausen, 13	3.5 ± 0.1	L. Imb.	Eratos.	6800 ± 900	−4.5 ± 0.3	0.7–2.5	Likely
Ioffe, 8	3.6 ± 0.1*	L. Imb.	L. Imb.	7100 ± 2900	−5.0 ± 0.7	0.6–2.0	Not likely
La Pérouse, 28	3.6 ± 0.1	L. Imb.	L. Imb.	8500 ± 2600	−5.5 ± 1.1	0.8–6.0	Likely
McLaughlin, 10	3.7 ± 0.1	L. Imb.	Imbr.	8600 ± 2800	−5.0 ± 0.8	0.7–3.0	Not likely
Coulomb, 5	3.7 ± 0.1	L. Imb.	L. Imb.†	8900 ± 2100	−5.3 ± 0.5	0.6–7.0	Not likely
Robertson, 12	3.7 ± 0.1	L. Imb.	Coper.	9400 ± 2900	−4.3 ± 0.6	0.6–2.0	Likely
Pitiscus, 19	3.8 ± 0.1	E. Imb.	Imbr.†	12,600 ± 2900	−4.9 ± 0.5	0.7–10.0	Not likely
Paracelsus, 38	3.8 ± 0.1	E. Imb.	Imbr.†	12,700 ± 2800	−3.8 ± 0.4	0.6–2.5	Not likely
Al-Biruni, 27	3.8 ± 0.1	E. Imb.	Imbr.	13,200 ± 2900	−5.1 ± 1.0	0.8–9.0	Not likely
Birkeland, 39	3.8 ± 0.1	E. Imb.	Eratos.	13,700 ± 3000	−3.6 ± 0.3	0.7–4.0	Possibly
Lobachevskiy, 34	3.8 ± 0.1	E. Imb.	L. Imb.	16,000 ± 3100	−3.9 ± 0.3	0.7–3.0	Likely
Vestine, 26	3.8 ± 0.1	E. Imb.	Imbr.	16,200 ± 2900	−3.5 ± 0.4	0.7–8.0	Not likely
Hahn, 25	3.8 ± 0.1*	E. Imb.	L. Imb.	16,400 ± 5000	−2.8 ± 0.5	0.7–3.0	Possibly
Icarus, 2	3.8 ± 0.1*	E. Imb.	Imbr.†	17,200 ± 4000	−5.5 ± 0.5	0.7–3.5	Possibly
Manzinus, 22	3.8 ± 0.1*	E. Imb.	Imbr.†	17,700 ± 3100	−5.3 ± 0.4	0.6–3.0	Not likely
Bose, 3	3.8 ± 0.1	E. Imb.	Imbr.†	19,200 ± 2800	−4.0 ± 0.2	0.7–6.0	Not likely
Arnold, 15	3.8 ± 0.1	E. Imb.	L. Imb.	19,500 ± 2100	−5.3 ± 0.4	0.9–11.0	Not likely
Tikhov, 35	3.8 ± 0.1*	E. Imb.	Nectar.	20,000 ± 5200	−2.2 ± 0.5	0.8–4.0	Not likely
Baillaud, 14	3.9 ± 0.1	Nectar.	L. Imb.	21,400 ± 2200	−4.3 ± 0.3	0.7–14.0	Not likely
Piccolomini, 18	3.9 ± 0.1*	Nectar.	Imbr.	24,600 ± 4100	−3.7 ± 0.4	0.8–2.5	Possibly
Roberts, 1	3.9 ± 0.1*	Nectar.	Im./Ne.†	25,200 ± 4100	−3.5 ± 0.3	0.7–10.0	Not likely
Bridgman, 33	3.9 ± 0.1*	Nectar.	Imbr.†	27,300 ± 5800	−4.6 ± 0.7	0.7–1.7	Possibly
Vlacq, 20	3.9 ± 0.1	Nectar.	Imbr.	27,900 ± 4200	−3.6 ± 0.4	0.8–4.0	Not likely
Ansgarius, 29	3.9 ± 0.1*	Nectar.	Imbr.†	29,300 ± 4700	−3.4 ± 0.4	0.9–4.0	Possibly
Laue, 11	3.9 ± 0.1*	Nectar.	Imbr.	31,600 ± 5500	−4.4 ± 0.6	0.8–9.0	Not likely
Joule, 6	4.0 ± 0.1*	Pre-Ne.	Im./Ne.	31,300 ± 5500	−2.9 ± 0.3	0.8–4.0	Not likely
Freundlich, 37	4.0 ± 0.1	Pre-Ne.	Imbr.†	32,800 ± 4200	−2.7 ± 0.2	0.8–6.0	Not likely
Neumayer, 30	4.0 ± 0.1*	Pre-Ne.	Nectar.	33,300 ± 4700	−3.6 ± 0.3	0.8–5.0	Not likely

<sup>a</sup> Assigned number in Fig. 1 and Table 2.

<sup>b</sup> In Ga with 1 $\sigma$  error. See text for detailed description of computation and “\*” notation.

<sup>c</sup> Epoch associated with model ages using divisions suggested by Stöffler et al. (2006).

<sup>d</sup> Epoch estimated in USGS Geologic Atlas of the Moon. See text for details and definition of “+” notation.

<sup>e</sup> Observed cumulative crater density per 10<sup>6</sup> km<sup>2</sup> at  $D = 1$  km. Error is  $\sqrt{N_{cum}/area}$ .

<sup>f</sup> Differential slope of the SSC SFD for diameter range (km) in next column.

<sup>g</sup> Indicates if CF is plausibly original (“likely” and “possibly”) or has been resurfaced (“not likely”).

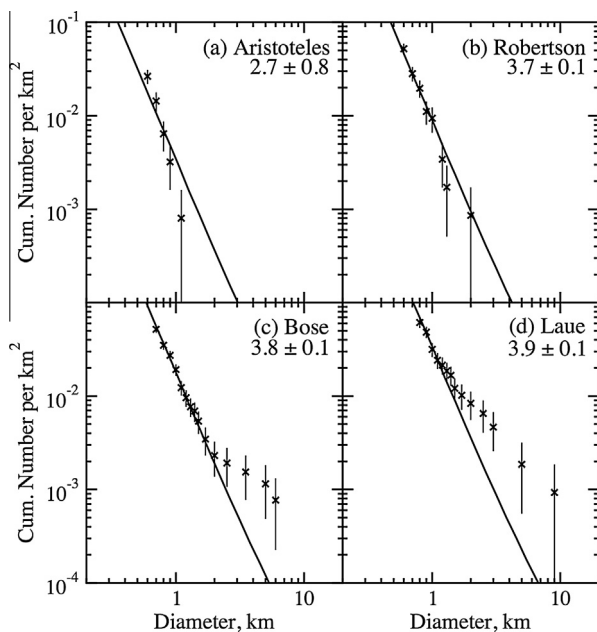


**Fig. 6.** Examples from Table 4 of good fits to SSC SFDs (x's) by the MPF (solid line) over a wide range of ages. Ages with 1 $\sigma$  errors of the associated CFs are indicated. See text and Fig. 5 for detailed description of fit analysis.

bodies has been constant for 3.5–3.2 Ga because a log–log plot of crater density per square kilometer vs. age yields a line.

With that said, we are careful to report our crater densities in Table 4, which can be attached to any derived chronology that comes up in the future. Moreover, we are only using the available and fairly well established chronologies found in the literature (Marchi et al., 2009; Neukum et al., 2001); no alternative chronology yet exists beyond these ones so far. In addition, while one could argue the lunar impact flux might experience huge variations between the tie points near the present and at ~0.11, ~0.8, ~3.5–3.2 Ga, there is no logical reason why it should do so, at least if we use main belt evolution models as a guide. At best, we argue this simply introduces an uncertainty factor of about ~2 into our derived ages, with the factor of 2 set by the variation in crater density between the chronology tie points. Because the derived chronologies are arguably only good to factor of 2 anyway (Marchi et al., 2009), we believe we are showing reasonable caution in our interpretation.

Asymmetric errors for the age were also calculated using the 50% values around the  $\chi^2$  minimum. However, because of uncertainties in the MPF beyond just the Poisson statistics associated with the  $\chi^2$  fit (e.g., in the production function shape) and in the calibrations of the crater counts with radiometric ages (Marchi et al., 2009), we argue that these are minimum errors. In particular, we argue that any production function and chronology cannot

**Table 5**

Small, superposed crater size–frequency distributions that are not consistent with the Model Production Function.

Crater name	USGS epoch	Relative crater densities	$b$	$D$ range	Original floor
Rosenberger, 21	Nectar.*	17,200 ± 3100	−2.4 ± 0.3	0.7–6.0	Not likely
Mezentsev, 4	Im./Ne.*	23,100 ± 3400	−2.3 ± 0.2	0.7–7.0	Not likely
Millikan, 32	Im./Ne.	29,400 ± 3800	−3.2 ± 0.3	0.8–13.0	Possibly
Shayn, 36	Im./Ne.	46,400 ± 5800	−2.8 ± 0.2	0.7–8.0	Not likely

See Table 4 and text for description of columns.

estimate the absolute model age to better than 0.1 Gyr. Therefore, we computed a more appropriate error based upon the original output of the  $\chi^2$  fit as follows. First, to simplify presentation of the data we averaged the asymmetric  $\chi^2$  fit errors to generate a Gaussian (symmetric) error. Then, the average was straightforwardly rounded up to the nearest tenth of a Gyr.

Finally, we note that the MPF has given us the set of ages reported in Table 4. However, these values will change if there are alterations to the production function (Morbidelli et al., 2012) or the chronology. Therefore, the ages presented here should be considered provisional.

### 3. Results

Table 4 summarizes the information compiled for each of the SSC SFDs that are fit well by the MPF (e.g., Fig. 6), which is for a majority of our CFs (36 out of 40). The first column indicates the CF associated with the SSC SFD, along with number assigned to the CF in Fig. 1. The first value is the computed model age of the CF in Ga, along with the error. The ages marked by an “\*” are more uncertain due to presence of many secondaries, or poor statistics related to small numbers of craters and/or counting areas (discussed in more detail below). Table 4 is organized first by the youngest to oldest absolute model age, then by the youngest to oldest relative cumulative density (column 5). The next column contains the lunar epoch associated with the model age estimated by this work of the CF (column 2) using the ranges proposed by Stöffler et al. (2006). This was done to facilitate comparison with previous work, since most CFs analyzed previously have only a formation epoch available, not any absolute ages. These previously assessed formation epochs, obtained from the USGS Geologic Atlas of the Moon, are given in the 4th column. We also surveyed Wilhelms’ (1987) maps to determine if there were any disagreement in the formation epoch. There were ~30% that Wilhelms estimated to be older than in the USGS maps (marked with “+”). In column 5, the SSC SFD relative crater density at  $D = 1$  km and its associated error is given to help better refine the age of the CFs within the larger absolute model age groupings (column 2), and for application with other production functions/chronologies. The 6th column contains the differential slope,  $b$ , and error for the diameter range of the SSC SFDs given in the next column. In this work, crater SFDs that are termed “steep” have  $b \leq -3.5$ , and a relative crater density that decreases with increasing diameter on an  $R$ -plot. Crater SFDs with  $b = -2.5$  to  $-3.5$  are termed “flat”, related to the roughly horizontal shape they have on  $R$ -plots where the relative density increases or decreases very little with increasing diameter. Lastly, crater SFDs with  $b \geq -2.5$  are termed “shallow”, for which crater density increases with increasing diameter on the  $R$ -plot. The final column indicates whether, by qualitative observation, CFs are considered to be original (“likely”) or greatly modified by later geological processes (“not likely”). For example, observations of visible hummocks and deep crater walls support an original CF, while observations of dark smooth material, suggestive of later volcanic resurfacing, support a modified CF. “Possibly” notation indicates there is evidence that the crater floor is original, but it is not as con-

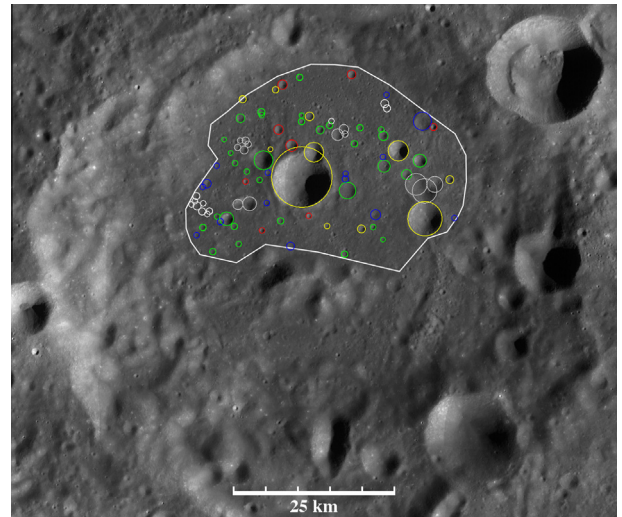


**Fig. 7.** Laue crater ( $D = 89$  km,  $28^\circ\text{N}$ ,  $97^\circ\text{W}$ ). This is one of the several CFs that have small counting areas, which produce poor statistics for the SSC SFDs. The counting area (within white outline) is  $1080$  km<sup>2</sup>. Also shown are the SSCs measured in various colored circles (designations as described in Fig. 3). North is up and scale is indicated. Another example, Vavilov, is shown in Fig. 2a, with a counting area of  $840$  km<sup>2</sup>.

clusive. These are included with the “likely” category when the two types of floors are discussed.

Four of the SSC SFDs are not fit well by the MPF. These are given in Table 5 and shown with respect to the MPF in Fig. 12. The columns are generally the same as in Table 4, but we do not report an age or Stöffler epoch for these CFs because the SSC SFDs are not consistent with the MPF. Specifically, these SFDs are shallower than the MPF for a considerable portion of the diameter range. We discuss likely reasons why these SSC SFDs are different from the MPF in Section 4.

#### 3.1. Crater floor model ages

As stated above, CF model ages with a “\*” are noted because their ages are more uncertain due to various factors. One issue, which is specific to younger CFs (Vavilov, Hayn, Aristoteles, Theophilus, Geminus, Hale), is poor statistics for the SFDs due to the fewer SSCs that formed. Another issue is measuring SSCs within small areas (e.g., Figs. 2a and Fig. 7), which also produces poor statistics for several SFDs (Vavilov –  $837$  km<sup>2</sup>, Hale –  $663$  km<sup>2</sup>, Langmuir –  $650$  km<sup>2</sup>, Ioffe –  $851$  km<sup>2</sup>, Hahn –  $671$  km<sup>2</sup>, Icarus –  $1106$  km<sup>2</sup>, Tikhov –  $751$  km<sup>2</sup>, Bridgman –  $841$  km<sup>2</sup>, Joule –  $1053$  km<sup>2</sup>, Laue –  $1076$  km<sup>2</sup>). A final issue is if the number of OSs recorded is a considerable fraction (qualitatively) of the total SSCs, then identification of any primary SSCs is more uncertain. For these, when the OSs are included as part of the “primary” SSC SFD, the calculated CF age or the SFD shape are significantly changed (e.g., Fig. 8). For example, Vavilov CF age increases appreciably

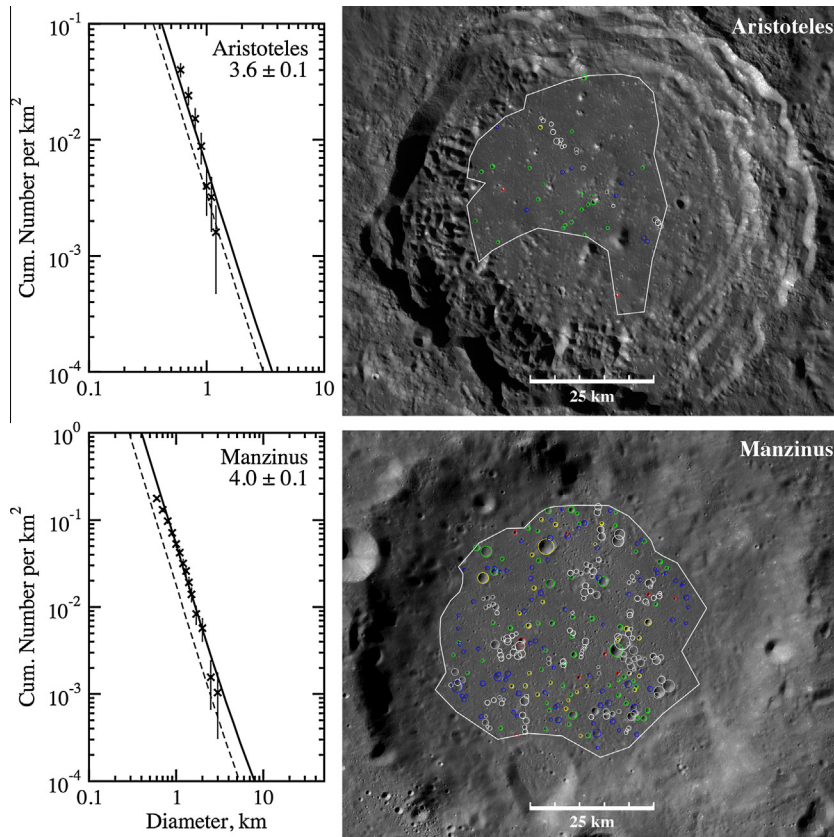


**Fig. 8.** Examples of SSC SFDs that are considerably affected by OSs. Shown are Aristoteles ( $D = 88$  km,  $50^\circ\text{N}$ ,  $17^\circ\text{E}$ ) and Manzinus ( $D = 98$  km,  $68^\circ\text{S}$ ,  $26^\circ\text{E}$ ). Rightmost are the MPF fits (solid line) to the SFDs with OSs included (x's). These can be compared with the MPF fits for the same SSC SFDs without OSs included represented by the dashed line. Note the  $x$  and  $y$  scales are different for each plot. On the left are the SSC measurements (colored circles) on each CF, with colors having the same designation described in Fig. 3. Most important to observe is the fraction of white/gray circles (OSs) to colored circles ("primaries"), which is generally significant. North is up in both images and scale is indicated.

from  $\sim 1.7 \pm 0.1$  to  $\sim 2.3 \pm 0.4$  Ga when the OSs identified are added. Other CFs influenced by an abundance of OSs are Aristoteles, Theophilus, Geminus, Icarus, Manzinus, Tikhov, Piccolomini, Roberts, Ansgarius, and Neumayer (e.g., Fig. 8).

With these caveats in mind, we plot the CF model ages and their  $1\sigma$  errors (Table 4) as probability Gaussians to produce Fig. 9. The plot ends at 1 Ga and 4 Ga because of the limitation of our technique for youngest and oldest terrains, as discussed earlier. Moving up on the  $y$ -axis indicates a higher (linear) probability of observing that surface age. The ages are divided into two datasets, one representing those with possible original CFs (Fig. 9a) and those that have likely been resurfaced (Fig. 9b). The dashed lines are for the individual CFs (some age histograms overlap, so the number of CFs represented by a Gaussian is shown above that Gaussian), and the solid lines are the sums. The solid line for original crater floors characterizes the trend for crater formation, while interpretation of the solid line for resurfaced crater floors is more complex (see Section 4). Also shown in the background is a traditional histogram of the CF mean ages. In general, impacts and resurfacing are suggested to occur more frequently for ages older than 3.0 Ga, while these geological processes are suggested to be sporadic for younger ages.

It is interesting to compare the Stöffler epochs (Table 4, column 3) representing our work with previous work represented by the USGS epochs (Table 4, column 4). Many of the CFs appear to be older in our work. This is especially true for the previously classified Copernican aged craters, which all have Eratosthenian or Imbrian ages here.

### 3.2. Analysis of small, superposed crater size–frequency distributions

The shapes of the SSC SFDs appear to be constant with time for  $D < 3$  km, at least in the age range observed. This is illustrated in Fig. 10, which plots several example SFDs in  $R$ -plot format with steep slopes that are concordant within error. The gray shaded area covers  $D \geq 3$  km, where data have poor statistics.

Taking a more detailed look at the OS SFDs indicates they have a wide variety of differential slopes,  $b$ , from  $\sim -1$  to  $-10$  (Table 6, Fig. 11). Table 6 also indicates there may be a correlation between differential slopes and cumulative density of the OS SFDs. The highest crater densities all have slopes around  $-3$  to  $-4$ . However, we have not found any significant correlation between OS SFD slopes and location or age. Meanwhile, it is interesting that several OS SFDs have similar slopes to the "primary" crater SFDs from the same CF (indicated by a "\*" in column 2 of Table 6). As a final result, when all the OS SFDs are combined to get an average, we find that this SFD has  $b \sim -3.7$ , similar to the power-law slope previously determined for the average secondary crater population on the Moon (e.g., McEwen and Bierhaus, 2006).

## 4. Discussion

A foremost observation is that a majority of our SSC SFDs are consistent with the MPF. This has important implications. The MPF is derived from numerical models and observations of relevant impactor populations for the Moon (Marchi et al., 2009).

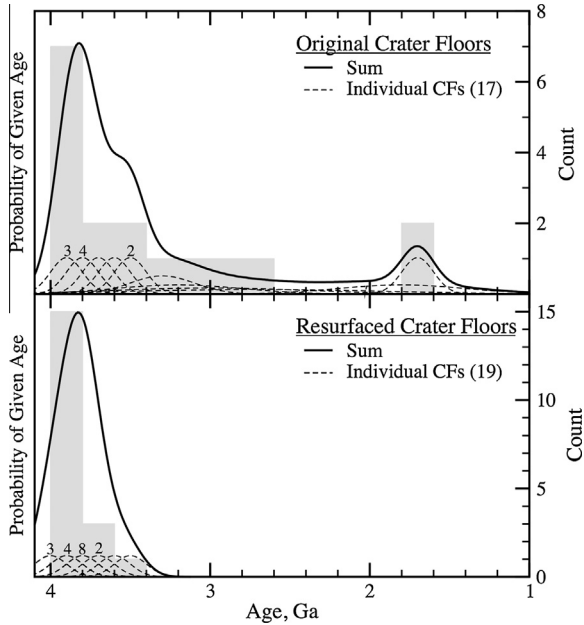


**Fig. 9.** Gaussian and traditional histograms of (a) original CF ages and (b) resurfaced CF ages (Table 4). Probability Gaussians for each individual CF (dashed) center on the mean age and  $1\sigma$  error defines the width and are linear in scale with probability of that ages increasing along the y-axis. Some CFs have the same ages and errors, therefore their Gaussians overlap and the numbers over these indicate how many are represented. Solid lines represent the sums of the Gaussians for each relevant group. Gray columns are the mean ages shown as a traditional histogram and the right axis displays the counts.

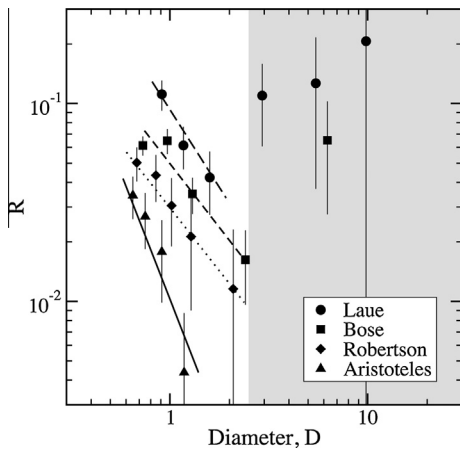


**Fig. 10.** Relative ( $R$ ) plot of select SSC SFDs from Table 4. A CF is shown to represent each lunar epoch. Lines are drawn (not rigorous fits) to illustrate that the SSC SFD slopes do not change significantly within error through time for  $D = 0.6\text{--}3$  km. In the shaded box on the right side of the plot the SFD shape is poorly known due to the small sample of craters.  $R$ -plots are generated through dividing the differential crater SFD by one with  $b = -3$ . Data are plotted using log–log values and  $\sqrt{n_{bin}/area}$  error bars are shown, where  $n_{bin}$  is the number of craters in each bin. SSC SFDs correspond to those shown in Fig. 6.

Therefore, it pertains only to formation of primary craters, not secondaries. The similarity of many of our SSC SFDs to the MPF may indicate that we have little contamination by unrecognized secondaries for these CFs. However, we have evidence that secondaries can have crater SFDs similar to the MPF in this diameter range. For instance, some CFs have OS SFDs that are similar to the “primary” crater SFDs, which are consistent with the MPF (cf. slope,  $b$ , in Table 6 to Table 4). On the other hand, SSC SFDs with no rec-

**Table 6**  
Characteristics of obvious secondaries size–frequency distributions.

Crater name	$b$	$D$ range	Observed crater density <sup>a</sup>
Roberts, 1	$-0.7 \pm 0.8$	0.7–2.0	$14,600 \pm 3100$
Pitiscus, 19	$-1.5 \pm 1.4$	0.7–1.7	$5000 \pm 1800$
Rosenberger, 21	$-1.9 \pm 0.4^*$	0.7–3.4	$7700 \pm 2100$
Bose, 3	$-1.9 \pm 0.6$	0.7–1.6	$7300 \pm 1700$
Aristoteles, 16	$-2.3 \pm 1.0$	0.6–1.3	$3200 \pm 1600$
Vestine, 26	$-2.3 \pm 1.3^*$	0.7–1.6	$2000 \pm 1000$
Shayn, 36	$-2.4 \pm 1.6^*$	0.7–1.4	$3500 \pm 1600$
Paracelsus, 38	$-2.7 \pm 0.6^*$	0.6–2.2	$9700 \pm 2400$
Millikan, 32	$-2.7 \pm 0.4$	0.8–4.0	$26,500 \pm 3500$
Neumayer, 30	$-2.9 \pm 0.2$	0.8–3.8	$73,000 \pm 6800$
Laue, 11	$-3.0 \pm 0.8^*$	0.8–4.0	$14,900 \pm 3700$
Manzinus, 22	$-3.1 \pm 0.3$	0.6–3.0	$35,300 \pm 4300$
Vlacq, 20	$-3.1 \pm 0.4^*$	0.8–2.8	$19,200 \pm 3500$
Joule, 6	$-3.1 \pm 0.8^*$	0.8–2.0	$17,100 \pm 4000$
Hausen, 13	$-3.4 \pm 0.7^*$	0.7–2.3	$1000 \pm 300$
Ansgarius, 29	$-3.4 \pm 0.5^*$	0.9–2.7	$24,200 \pm 4200$
Bridgman, 33	$-3.6 \pm 0.9^*$	0.7–1.7	$10,700 \pm 3600$
Icarus, 2	$-3.7 \pm 0.8$	0.7–1.7	$9000 \pm 2900$
Robertson, 12	$-3.8 \pm 0.9^*$	0.6–1.3	$5100 \pm 2100$
Tikhov, 35	$-3.8 \pm 2.0^*$	0.8–1.8	$8000 \pm 3300$
Arnold, 15	$-3.9 \pm 1.1^*$	0.9–2.7	$2000 \pm 700$
Theophilus, 17	$-4.0 \pm 0.8^*$	0.6–1.3	$2300 \pm 1300$
Coulomb, 5	$-4.1 \pm 0.6$	0.6–1.3	$2500 \pm 1100$
Freundlich, 37	$-4.3 \pm 1.2$	0.8–1.6	$3200 \pm 1300$
Al-Biruni, 27	$-4.4 \pm 1.3^*$	0.8–1.4	$6900 \pm 2100$
Geminus, 24	$-4.7 \pm 1.8^*$	0.7–1.3	$1900 \pm 1400$
Piccolomini, 18	$-5.3 \pm 1.2^*$	0.8–1.5	$8000 \pm 2300$
Baillaud, 14	$-5.7 \pm 0.6$	0.8–1.8	$8600 \pm 1400$
Lobachevskiy, 34	$-8.2 \pm 2.8$	0.7–0.9	$400 \pm 400$
Ioffe, 8	$-10.6 \pm 4.0$	0.6–1.3	$3000 \pm 1800$
Average	$-3.7 \pm 0.1$	0.9–4.0	N/A

A “\*” notation indicates that the slope of the OSs match the slope of the assumed primary SSC population for this CF within error. See Table 4 and text for description of columns.

<sup>a</sup> Indication of OS density identified on the CF, not relative age.

ognized secondaries (Hayn, Hale, Langmuir, and Lyman) are consistent with the MPF, and a several CFs have OS SFDs that are dissimilar to the “primary” SSC SFD and the MPF.

#### 4.1. Crater floor model ages

Several noteworthy findings are revealed upon examining the distribution of original CF ages (Fig. 9a, Table 4). First, the results of a Kolmogorov–Smirnov ( $K-S$ ) routine available in the statistical package  $R$  (<http://www.r-project.org/>) comparing the cumulative distribution of these ages to the assumed chronology function indicate that the distributions are different with 89% confidence level (maximum distance between the distributions,  $D_{K-S} = 0.2797$ ). Because the assumed chronology function is suggested to represent the small impactor flux (as discussed in the Section 2), this difference means that the large impactor flux does not necessarily correlate with the small. This result might be viewed as curious. For example, our expectation would have been that small and large lunar impactors “walk together” in the same crater SFD. In other words, if the impact flux of small lunar projectiles were constant over time, the age distribution of the larger projectiles should also be uniform over the last several billion years. This apparent difference is therefore interesting. How might this difference in flux be explained?

A possibility could involve the so-called E-belt, a putative extension of the primordial main belt that became unstable at the time of the LHB about 4 Ga (Bottke et al., 2012). This population, originally located between 1.7 and 2.1 AU, arguably dominated the production of very large craters on the Moon from 4 to 1 Ga. Preliminary work shows that the width of this region in semi-major axis is narrow enough that small E-belt objects often escape

more rapidly into resonances via Yarkovsky drift. Once in resonance, the objects can eventually evolve onto orbits where they can hit the Moon. Because larger objects evolve more slowly by Yarkovsky drift, they take longer to escape the E-belt region and thus decay more slowly. Accordingly, the ratio of small/big projectiles from the E-belt is probably higher in the early days of the LHB than at much later times. The interesting issue here is that at later times, the largest E-belt projectiles may continue to dominate the flux from the main belt, but this may not be true for the smallest projectiles.

Another possibility is that the flux of multikilometer projectiles escaping the main belt may have been more time-dependent than the smallest projectiles, and therefore could have been more susceptible to being influenced by family-forming events. As an example, consider the breakup of the Flora family along the inner edge of the main belt. While this breakup may have only nominally influence the lunar impact flux for objects a few tens of meters in diameter, which could have been drawn from a broad swath across the main belt, a surge of multikilometer bodies might have dominated the local population entering the  $v_6$  resonance near 2.1–2.2 AU. This could have therefore lead to a mismatch in the flux rate between small and large bodies.

We also find that a declining flux is observed extending  $\sim 1.0$  Gyr after the heaviest bombardment ( $\sim 3.8$  Ga in our data). Since this curve represents lunar impact bombardment, the declining flux may represent an extended tail for the LHB for  $D \sim 90$  km craters until  $\sim 3.0$  Ga. Because the assumed chronology function suggests the exponential decay of the small crater flux only extends to  $\sim 3.5$  Ga, this may be the primary cause for the difference in the distributions revealed by the K–S test. The lack of ages older than 3.8 Ga is due to our exclusion of older terrains as previously discussed.

Furthermore, we find that relatively few impacts are observed for ages younger than  $\sim 3$  Ga (at least until  $\sim 1$  Ga, where our dataset is inapplicable, see Section 2), which would be expected from the chronology. However, these preliminary data hint that the ages may not be randomly distributed. No CFs with ages between 2.6–1.9 Ga and 1.6–1.0 Ga are observed in these data. Meanwhile, two CFs appear to have formed within a couple hundred million years around 1.8 Ga. Therefore, this (incomplete) distribution of ages may be somewhat suggestive of a bombardment flux for the Moon's middle age with “lulls” and “spike(s)”, at least for the relatively large objects that formed these CFs. However, because the CFs examined are only a sample ( $\sim 38\%$ ) of the total number between  $D = 80$ –100 km, the histograms in Fig. 9a do not represent the full impact history, and the K–S test results are inconclusive for this age range. Future work will compile superposed crater densities on *all* other “Copernican” and “Eratosthenian” aged CFs as identified in the USGS Geological Maps of the Moon of these diameters to obtain the complete recent bombardment flux and determine if the hint here of lulls and spike is real. This work will also perform further statistical analysis of the significance of any spikes or lulls found relative to a constant flux.

Finally, we find that the model ages computed here, as represented by the Stöffler epochs in Table 4, are sometimes older than estimated by previous work, as represented by the USGS epochs. Some CF ages do match the original estimated epochs, but these are generally older surfaces. However, a majority of the younger surfaces (Late Imbrian and younger) are the ones that our work finds to be older. There are several possible methodological concerns behind this disagreement including: inaccuracies in age classification on USGS maps and other previous work (e.g., Wilhelms, 1987), uncertainty in the Stöffler epoch boundaries (Stöffler et al., 2006) and/or inaccuracies in the MPF and the chronology. The most interesting and probable of these is that previous estimation of the formation epochs (e.g., USGS Geologic Atlas of the Moon, Wilhelms,

1987) is inaccurate. First, Lunar Orbiter images, which were the primary source, have poor resolution, especially away from the near side where most of the craters we examined are located. It was likely difficult to really determine how fresh a crater rim or ejecta blanket/rays are. Therefore, while these images were the best for a long time, especially for recognizing crater features, the new LROC images have vastly improved on them. Second, because of the previously poor resolution coverage for most of the craters we examined, direct superposed crater counts were not possible. Therefore, a technique often used was the  $D_L$  parameter, which relied on qualitative observations of the degradation states of the craters. Subsequent analysis has since shown that this technique is unreliable (e.g., Hiesinger et al., 2000), primarily because the degradation process is still not well understood, and has been discovered to be highly variable and dependent on location. If the previous estimations are in error, then several of the CFs previously cataloged to be Copernican and Eratosthenian epoch may actually be older and part of the “tail” after the LHB. If this is the case, then it further hints, with less craters forming in the latest epochs, that there could be lulls in impact cratering between  $\sim 3$  and 1 Ga for the large impactors that formed these CFs.

However, we cannot rule out that there are issues with the MPF that may be causing these discrepancies. One primary issue is that the chronology used to compute the ages may be inaccurate. The chronology is based upon associating observed crater densities of the Apollo landing sites to the radiometric ages found for the samples brought back from those sites. As discussed in the Introduction, there are several potential issues related to this technique. First, the representative areas chosen for the crater counts may not correspond to the sample analyzed. Areas could be too small, too big, or cover the wrong geological units. Second, there are very few samples collected and examined for most of the age range of interest here (4–1 Ga) to calibrate the chronology (e.g., Stöffler and Ryder, 2001). Third, the chronology assumes a constant cratering rate for this age range. Recent discoveries and modeling of asteroid break-ups in the MBA population indicate that impact rates may temporarily increase at random times throughout the last 3 Gyr (Bottke et al., 2007, 2008; Marchi et al., 2009; Nesvorný et al., 2002). However, research has not yet been able to indicate exactly when these occurred for our time frame of interest, and how big of a spike in lunar impacts these break-ups would have caused. Combining numerical models with observations of the MBA population and the cratering record on the Moon, like the one presented here, may eventually lead to refinement of when these spikes occurred and how large they were. For example, our data in Fig. 9a may indicate one of these “spikes” at  $\sim 1.8$  Ga, but it is based upon only two CFs, so we cannot be confident until these observations are verified by models and further data. In summary, these issues remind us that our calculated ages could be inaccurate, and may change with future improvements in the chronology.

#### 4.2. Analysis of small, superposed crater size–frequency distributions

We observe little change in the differential slopes of the SSC SFDs with time for  $D = 0.6$ –3 km (Fig. 10). This is the first strong indication, of which we are aware, of little variation to the shape of the SFD of the  $D \sim 10$ –80 m impactor population during the middle age of lunar bombardment history. This implies that collisional evolution and delivery mechanisms may have conspired to provide a source region that regularly supplied these small objects in these proportions. The match of our crater SFDs to the MPF is consistent with NEOs being the source for the SSC population.

Conversely, for SSCs above  $D \sim 3$  km, statistics are too poor to infer any characteristics for the SFDs (Fig. 10, shaded region). However, a transformation to shallower slopes extending toward the upper right in an  $R$ -plot is possibly observed for these SSC SFDs, which

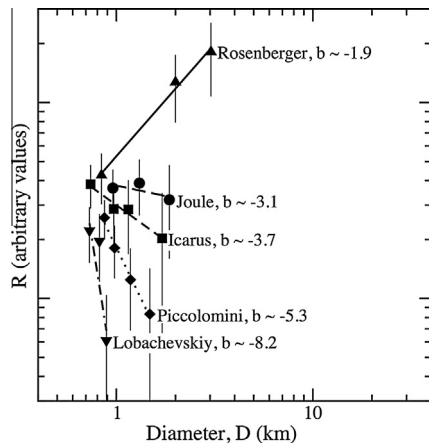


**Fig. 11.** R-plot illustrating the variability of OS SFD differential slopes,  $b$ , observed in this work. Curves have been shifted up and down the y-axis for clarity and the R-value is arbitrary. OS SFDs shown are examples selected from Table 6. R-plot details are as described in Fig. 10 and the text.

could be consistent with Population 1 observed by Strom et al. (2005). Furthermore, we did not observe any of our SSC SFDs transforming to steeper slopes and deviating below the MPF (see Section 2.4). Perhaps this is another indication that the hint of a transformation to shallower slopes for  $D > 3$  km SSCs is real and needs further investigation and is a subject of future work.

Results for the OS SFDs also are intriguing. We observe that their differential slopes,  $b$ , can vary considerably (Table 6, Fig. 11). Fundamentally, this suggests that SFDs of individual secondary crater fields can deviate from the steep differential slope ( $b \sim -4$ ) often stated for the average secondary crater population on the Moon (e.g., McEwen and Bierhaus, 2006). This has significant, but not wholly unexpected, consequences for understanding the formation of ejecta and secondary craters. Possibly terrain properties could be responsible (e.g., McEwen and Bierhaus, 2006). For example, if there were any correlation between slope and location and/or surface age, terrain properties might be implicated. However, we do not observe many correlations. The only potential correlation we found is that 4 OS SFDs on CFs in the equatorial western hemisphere (Laue, Joule, Icarus, and Robertson) have  $b = -3$  to  $-4$ . This is may be related to their proximity to Orientale (see below), and not likely an indication of unique terrain. Even so, this lack of correlation does not imply that terrain properties do not play a role in the variation (they likely do), just that the evidence may be subtle or confused by multiple cratering events (i.e., we do not know if the OSs measured represent one secondary field or many). Another possibility is that the variation in slope may also be a consequence of proximity to the source crater. Nearby secondary clusters and chains could have a different crater SFD than far-field clusters and chains (including debris that may actually orbit the Moon before impacting) (Gladman et al., 1995; McEwen and Bierhaus, 2006). However, we have not been able to determine if a correlation exists between proximity to source and slope, because we are not able to ascertain the source crater in most cases (even for the 4 CFs around Orientale, we are not certain Orientale is the source). The CFs analyzed here are typically in heavily cratered regions of the Moon, and just surrounded by too many possible sources that are all likely contributing.

There may be a correlation between differential slopes and cumulative density of the OS SFDs. Values in Table 6 indicate that the SFDs with the highest crater density all have slopes around  $-3$  to  $-4$ . However, this is not likely related to formation mechanisms, but more so to the idea that as more secondaries accumulate the slope should approach the  $-4$  value previously suggested for the average secondary crater population on the Moon (e.g., McEwen

and Bierhaus, 2006). This is further supported by the  $b = -3.7$  value obtained when all the OS SFDs are combined to get an average (Table 6).

#### 4.3. Analysis of small, superposed crater size–frequency distributions not consistent with the Model Production Function

We observe 4 CFs (10% of the total) with SSC SFDs that are not consistent with the MPF over a substantial diameter range: Rosenberger, Mezentsev, Millikan, and Shayn (Table 5, Fig. 12). There are several possible causes for these suggested differences between the MPF and the data. One is that the crater SFDs have been affected by resurfacing. At smaller diameters, these SFDs have shallower slopes than the MPF (Fig. 12). Resurfacing is a geologic process that tends to shallow crater SFDs through preferential erasure of small craters. Such resurfacing could be due to burial by subsequent crater ejecta, collapses (landslides) along the crater wall and peak due to seismic shaking, and/or subsequent mare-type volcanism. Because these are all older surfaces, as indicated by the higher crater densities, and we have already noted that these craters likely have resurfaced floors, considerable resurfacing by any or all of these mechanisms is plausible. Resurfacing is further supported by observed partially buried large superposed craters and by the fact that these SSC SFDs are dominated by degraded craters (Fig. 13).

Another possibility is secondary cratering. Not all secondaries form in clusters or chains, and unrecognizable ones may influence these SSC SFDs. However, secondary crater populations are not typically thought to have shallow slopes. Yet, as already discussed above, several of our OS SFDs do have shallow slopes, including those for Rosenberger, Millikan, and Shayn (Table 6, Fig. 11). Therefore, shallow secondary crater SFDs may be very possible, especially for small analysis areas and in isolated groups.

Another, less likely candidate for these inconsistencies between the data and MPF, is that a different impactor population is represented. For example, Strom et al.'s (2005) Population 1 has a shallow slope for  $D < 80$  km. However, telescopic observations of the impactor population assumed to be associated with this crater population, MBAs, do not yet extend to such small asteroids to confirm if it is shallow for these small diameters. Furthermore, we cannot assume that even if the small diameter range of the MBA population is currently shallow that it has not changed since the earlier epochs that these observed SSC SFDs represent. Finally, these CFs are not spatially or temporally isolated from CFs with SSC SFDs consistent with the MPF. Their  $D = 1$  km cumulative densities place them within the age range computed for the older CFs in Table 4 (Shayn is an exception). Therefore, there is no good evidence why these crater floors should record or retain unique impactor SFDs.

A final possibility is that different scaling laws could be used to generate alternate MPFs (Marchi et al., 2011). As mentioned in Section 2, the MPF presented so far in this work has used only the Pi-scaling law for the gravity regime (Schmidt and Housen, 1987) as given by the formulation of Melosh (1989, p. 118–119). However, the shape of the MPF depends on the scaling law chosen (Marchi et al., 2011; Wünnemann et al., 2012). In particular, if the terrain is harder, then the strength regime for impact cratering physics becomes relevant for larger diameters, possibly into the range studied for the SSCs. Therefore, a preliminary fit incorporating the strength regime was attempted for Millikan's SSCs. This fit used the scaling law developed by Holsapple and Housen (2007), with a hard rock strength of  $Y = 2 \times 10^7$  dyne  $\text{cm}^{-1}$ . In general, most of the scaling is still in the gravity regime, but SSCs with  $D < \sim 1$  km are now produced in the strength regime. This causes the MPF to become slightly shallower in this diameter range. However, even for our test case, Millikan, which has the least deviation from the MPF, the fit is not improved (cf. Fig. 14a to Fig. 12). Including only strength plainly does not change the MPF enough to account for

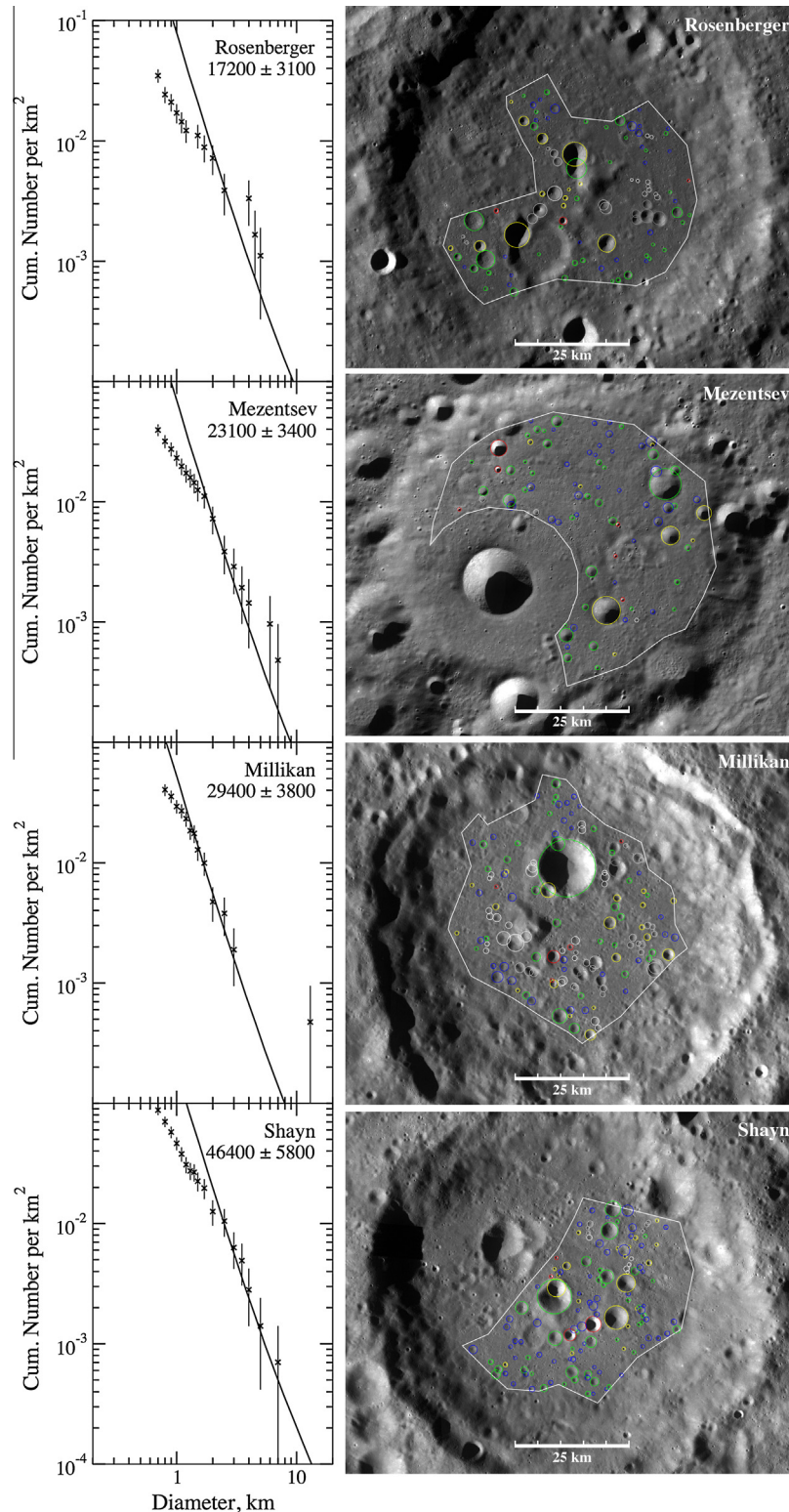


**Fig. 12.** SSC SFDs that are not fit well by the MPF: Rosenberg ( $D = 92$  km,  $56^{\circ}\text{S}$ ,  $43^{\circ}\text{E}$ ), Mezentsev ( $D = 85$  km,  $72^{\circ}\text{N}$ ,  $130^{\circ}\text{W}$ ), Millikan ( $D = 96$  km,  $47^{\circ}\text{N}$ ,  $121^{\circ}\text{E}$ ), and Shayn ( $D = 93$  km,  $33^{\circ}\text{N}$ ,  $172^{\circ}\text{E}$ ). Left column: SSC SFDs (x's) plotted with the closest MPF fit (solid line). These are considered poor because the MPF does not fit several data points, even within error. Values shown are the observed cumulative density per  $10^6$  km<sup>2</sup> for  $D \geq 1$  km and associated  $\sqrt{N_{cum}/area}$  error, where  $N_{cum}$  is the number of craters with  $D \geq 1$  km. Right column: Images of the crater floors with the SSCs measured represented by colored circles (designations as described in Fig. 3). North is up in all images and scale is indicated.

the deviation of small SSCs from the original MPF for these CFs. A more substantial change to the scaling law results from including layers of different strengths. This scaling law again used the Holsapple and Housen (2007) equation, but allows the strength to

change with depth (generally as a step function). A version with a thin, weaker layer ( $Y = 2 \times 10^7$  Pa and thickness is  $\sim 250$  m) on top of a stronger layer ( $Y = 2 \times 10^8$  dyne cm<sup>-1</sup>) was applied to Rosenberg, and the fit was greatly improved (cf. Fig. 14c to

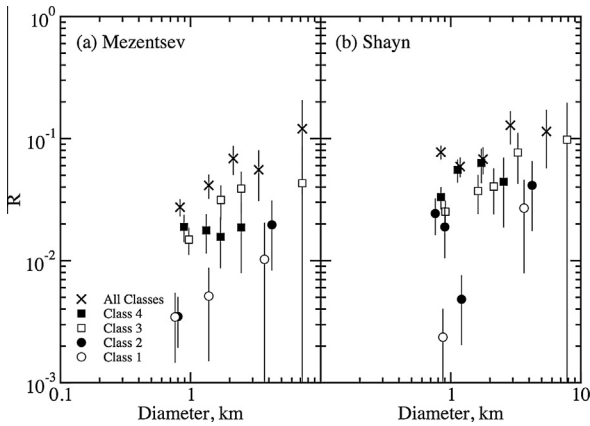


**Fig. 13.**  $R$ -plot of the SSC SFDs for (a) Mezentsev ( $D = 85$  km,  $72^\circ\text{N}$ ,  $130^\circ\text{W}$ ) and (b) Shayn ( $D = 93$  km,  $33^\circ\text{N}$ ,  $172^\circ\text{E}$ ). “All classes” SFD is shown (combines all the degradation classes, excluding OSs), along with the SFDs for each degradation class. The average  $R$ -value for each degradation class represents the relative proportions of SSC in each class, where larger  $R$ -values imply a larger proportion. Therefore, the SSCs on the floors of Mezentsev and Shayn are composed of a larger proportion of highly degraded craters.

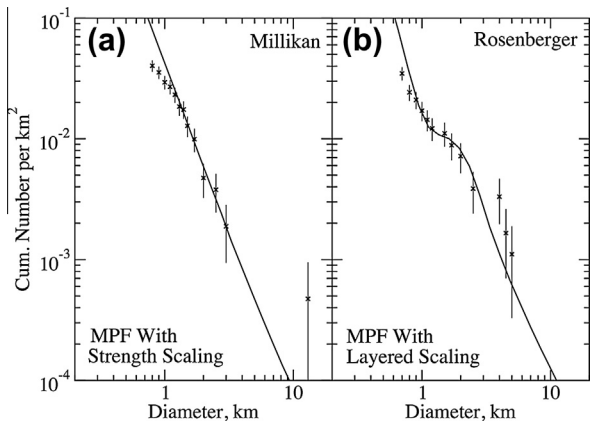


**Fig. 14.** Examples of new fits using alternate MPFs to the SSC SFDs of Millikan ( $D = 96$  km,  $47^\circ\text{N}$ ,  $121^\circ\text{E}$ ) and Rosenberger ( $D = 92$  km,  $56^\circ\text{S}$ ,  $43^\circ\text{E}$ ). (a) Millikan. The SSC SFD ( $x$ 's) fit by an MPF that incorporates the strength regime into the scaling law (solid line). The Holsapple and Housen (2007) scaling law with a hard rock strength of  $Y = 2 \times 10^7$  dyne  $\text{cm}^{-1}$  is used. This does not improve the fit (cf. Fig. 12), and we observe that incorporating strength alone does not significantly change the MPF. (b) Rosenberger. The crater SFD ( $x$ 's) fit by an MPF that incorporates a layered scaling law (solid line). The Holsapple and Housen (2007) scaling law with a thin, weaker layer ( $Y = 2 \times 10^7$  Pa and thickness is  $\sim 250$  m) on top of a stronger layer ( $Y = 2 \times 10^8$  dyne  $\text{cm}^{-1}$ ) is used. Here the fit is improved (cf. Fig. 12), but we do not yet have supporting observational evidence for a layered terrain.

Fig. 12). The other SSC SFDs inconsistent with the original MPF have not yet been tested, but this alteration to the MPF is promising. Meanwhile, it is hypothetically reasonable to assume that the geology of these crater floors is variable enough that employing different scaling laws is sensible. However, we do not have direct observational evidence to support their use. In future work, we will more thoroughly explore improving MPF fits using different scaling laws and search for observational evidence, such as layering in larger SSCs using LROC NAC images, to support their use.

## 5. Conclusions

This work has produced a new dataset of ages of 36 randomly located mid-sized CFs (see Table 1 for acronym definitions) that were formed during the Moon's middle age (4–1 Ga) (Table 4). Analysis

of the CF ages generated a plot of the formation frequency of large craters ( $D \sim 90$  km) on the Moon for this time period (Fig. 9a). Ages were calculated by applying the MPF (Marchi et al., 2009) to the density of SSCs  $D \approx 0.6$ – $15$  km measured using the LROC WAC global mosaic. Additionally, these craters were classified based upon degradation state (Fig. 4) and spatial distribution in clusters or chains (OSs) on the floors of the craters. Therefore, we also produced a new dataset of SFDs of small likely primary craters and likely secondary craters on the Moon (Tables 4–6). Compilation and analysis of these datasets suggest the following conclusions:

1. Most of the SSC SFDs compiled for our chosen CFs (36 of 40) are consistent with the shape of the MPF (e.g., Figs. 5 and 6 and Table 4). This implies that these SFDs are plausibly representative of the small primary impactor population, and are not heavily influenced by unrecognized secondaries.
2. A frequency histogram of the ages of these 36 CFs broadly indicates high bombardment rates and substantial resurfacing of the Moon's surface for the period older than 3.0 Ga, along with few impacts and relatively little resurfacing for younger ages (Fig. 9). Analyzing only the original CFs from the dataset that is consistent with the MPF (17 of 36; Fig. 9a), which specifically represent the bombardment history, we infer that tail of the LHB may have been extended until  $\sim 3$  Ga. After this time, there seem to be very few large impacts that may not be randomly distributed. The data hint a lull in the bombardment for 2.7–1.9 Ga and 1.6–1.0 Ga, with a possible spike in-between at  $\sim 1.8$  Ga. Future work will fully investigate this suggestion that the impact flux from 3–1 Ga could be characterized by lulls and spikes through calculating the ages of all craters of this size that may have formed in the Copernican and Eratosthenian.
3. Comparing our model ages of the CFs with previous work (USGS Geological Maps of the Moon, (Wilhelms, 1987) indicates that some CFs may be older than originally ascertained. This discrepancy in the estimated ages is observed frequently for the younger surfaces (Late Imbrian and younger). If this outcome is due to misidentifications by the previous work (several reasons have been presented earlier to support this), then we have further evidence that periods with no impacts are possible for 3–1 Ga. However, we cannot rule out inaccuracies in the MPF and/or uncertainty in the Stöffler epoch boundaries (Stöffler et al., 2006) as the potential cause.
4. SSC SFD slopes are suggested to be relatively stable for  $0.6 < D < 3$  km, at least for the Moon's middle age (Fig. 10). This implies that the  $D \sim 10$ – $80$  m impactor population was also stable for this period, and thus, that collisional evolution and delivery mechanisms consistently produce a source region (likely NEOs) with small objects in these proportions.
5. Our OS dataset shows a wide variety of differential slopes from  $b = -1$  to  $-10$  (Table 6, Fig. 11) for individual CFs. Provocatively, this is strong evidence that individual secondary crater SFDs can vary quite considerably, and are not always representative of the average asserted for whole lunar surface. We suggest these variations may be caused by one or both of these possibilities: changes in target material properties and/or proximity to the source crater (i.e., near-field secondaries could have a different SFD than far-field; McEwen and Bierhaus, 2006). However, unfortunately our data do not show any obvious correlations between differential slope and location and/or age that could be used to substantiate this conjecture.
6. Finally, four of the SSC SFDs are found to be inconsistent with the MPF (Table 5, Fig. 12). We propose several possible causes for these differences: the SFDs have been affected by resurfacing and/or unrecognized secondary craters, the SFDs represent a different impactor population than the NEOs, and/or the impact target properties are different requiring a different

scaling law for the MPF (e.g., Fig. 14). Of these the most likely is that resurfacing has affected these SSCs. This is supported by shallow slopes observed for these SFDs, as resurfacing tends to shallow crater SFDs through erasure of small craters, and the evidence in the images for resurfacing of these craters floors (Fig. 12), such as partially buried craters.

## 6. Supplemental Material

The Supplementary Material is an on-line database of backing figures and written notes about the analysis for each crater studied in this work (<http://data.boulder.swri.edu/~benke/michelle/craters/>). A folder is generated for each crater floor and includes (where “cratername” is a placeholder for the name of the crater and if -OS is appended to a filename that means that file is for the obvious secondary SFD):

- A plain text file of notes summarizing features of the crater such as age, counting area, and geology, and the process used in analyzing the crater. (cratername-read\_me.txt)
- Close up image of the mid-sized crater with no crater measurement markings. (cratername.png)
- Farther out image of the context around the mid-sized crater with the featured crater in the center. (cratername-context.png)
- Close up image of the measured small, superposed craters. As presented in the text, the “primary” crater degradation classes are represented by the following colors: Class 1 – red, Class 2 – yellow, Class 3 – green, and Class 4 – blue. The obvious secondary morphology classes are represented by: OS Class 1 – dark gray, OS Class 2 – medium gray, OS Class 3 – light gray, and OS Class 4 – white. (cratername-cc.png)
- Raw image of the MPF fit to the small, superposed crater size-frequency distribution. The left panel shows the fit along with the fit’s values of the crater density at  $D = 1$  km and associated error. The right panel shows the reduced  $\chi^2$  value, along with the computed age and its associated error. The error is determined from the +/- values indicated by the line above the minimum  $\chi^2$ . (cratername-age.png)
- R-plot of the total “primary” small, superposed crater size-frequency distribution, along with the distribution for each degradation class. (cratername-class.png)
- A plain text file of the results from the non-linear fit to compute the differential slope using the statistical package R. The error on b is the reported standard error divided by the reported residual standard error. (cratername-diff\_slope.png)
- Screenshots of the relevant sections of the USGS Geologic Atlas of the Moon displaying the previous work in determining the geology and age of the CF. (cratername-USGS\_geol.png and cratername-USGS\_geol\_desc.png)

## Acknowledgments

This work has been supported by the NASA Lunar Science Institute. We thank David Minton and anonymous reviewer for their comments that improved this manuscript.

## References

Arthur, D.W.G., Agnieray, A.P., Horvath, R.A., Wood, C.A., Chapman, C.R., 1963. The system of lunar craters, quadrant I. *Comm. Lunar Planet. Lab.* 2, #30.

Asphaug, E., Ryan, E.V., Zuber, M.T., 2002. Asteroid interiors. In: Bottke, W., Cellino, A., Paolicchi, P., Binzel, R.P. (Eds.), *Asteroids III*. pp. 463–484.

Baldwin, R.B., 1985. Relative and absolute ages of individual craters and the rate of infalls on the Moon in the post-Imbrium period. *Icarus* 61, 63–91.

Bottke, W.F., Morbidelli, A., Jedicke, R., Petit, J.-M., Levison, H.F., Michel, P., Metcalfe, T.S., 2002. Debaised orbital and absolute magnitude distribution of the near-Earth objects. *Icarus* 156, 399–433.

Bottke, W.F. et al., 2005a. The origin and evolution of stony meteorites. In: Knežević, Z., Milani, A. (Eds.), *Dynamics and Populations of Planetary Systems*. IAU Colloquium 197, pp. 357–374.

Bottke, W.F., Durda, D.D., Nesvorný, D., Jedicke, R., Morbidelli, A., Vokrouhlický, D., Levison, H.F., 2005b. Linking the collisional history of the main asteroid belt to its dynamical excitation and depletion. *Icarus* 179, 63–94.

Bottke, W.F., Nesvorný, D., Grimm, R.E., Morbidelli, A., O’Brien, D.P., 2006a. Iron meteorites as remnants of planetesimals formed in the terrestrial planet region. *Nature* 439, 821–824.

Bottke, W.F., Vokrouhlický, D., Rubincam, D.P., Nesvorný, D., 2006b. The Yarkovsky and YORP Effects: Implications for asteroid dynamics. *Annu. Rev. Earth Planet. Sci.* 34, 157–191.

Bottke, W.F., Vokrouhlický, D., Nesvorný, D., 2007. An asteroid breakup 160 Myr ago as the probable source of the K/T impactor. *Nature* 449, 48–53.

Bottke, W.F., Levison, H., Morbidelli, A., 2008. Understanding the impact flux on the Moon over the last 4.6 Gy. In: Presented at the Early Solar Sys. Imp. Bombard. I, Houston, TX, Abst. #3005.

Bottke, W.F. et al., 2012. An Archaean heavy bombardment from a destabilized extension of the asteroid belt. *Nature* 485, 78–81.

Boyce, J.M., Dial, A.L., 1975. Relative ages of flow units in Mare Imbrium and Sinus Iridium. In: *Lunar Sci. Proceedings*. Presented at the Lunar Sci. VI, pp. 2585–2595.

Burl, M.C., Merline, W.J., Colwell, W., Bierhaus, E.B., Chapman, C.R., 2001. Automated detection of craters and other geological features. Presented at the Int. Symp. Art. Intel., Rob., Auto. Space, Abst. #01-1008.

Chapman, C.R., Cohen, B.A., Grinspoon, D.H., 2007. What are the real constraints on the existence and magnitude of the Late Heavy Bombardment? *Icarus* 189, 233–245.

Cohen, B.A., Swindle, T.D., Kring, D.A., 2005. Geochemistry and  $^{40}\text{Ar}$ – $^{39}\text{Ar}$  geochronology of impact-melt clasts in feldspathic lunar meteorites: Implications for lunar bombardment history. *Meteorit. Planet. Sci.* 40, 755–777.

Craddock, R.A., Howard, A.D., 2000. Simulated degradation of lunar impact craters and a new method for age dating farside mare deposits. *J. Geophys. Res.* 105, 20387–20401.

Crater Analysis Techniques Working Group, 1979. Standard techniques for presentation and analysis of crater size–frequency data. *Icarus* 37, 467–474.

Čuk, M., Gladman, B.J., Stewart, S.T., 2010. Constraints on the source of lunar cataclysm impactors. *Icarus* 207, 590–594.

Čuk, M., Gladman, B.J., Stewart, S.T., 2011. Rebuttal to the comment by Malhotra and Strom on “Constraints on the source of lunar cataclysm impactors”. *Icarus* 216, 363–365.

Culler, T.S., Becker, T.A., Muller, R.A., Renne, P.R., 2000. Lunar impact history from  $^{40}\text{Ar}/^{39}\text{Ar}$  dating of glass spherules. *Science* 287, 1785–1788.

Farley, K.A., Vokrouhlický, D., Bottke, W.F., Nesvorný, D., 2006. A late Miocene dust shower from the break-up of an asteroid in the main belt. *Nature* 439, 295–297.

Fassett, C.I. et al., 2012. Lunar impact basins: Stratigraphy, sequence and ages from superposed impact crater populations measured from Lunar Orbiter Laser Altimeter (LOLA) data. *J. Geophys. Res.* 117, E00H06. <http://dx.doi.org/10.1029/2011JE003951>.

Gladman, B.J., Burns, J.A., Duncan, M.J., Levison, H.F., 1995. The dynamical evolution of lunar impact ejecta. *Icarus* 118, 302–321.

Hartmann, W.K., 2003. Megaregolith evolution and cratering cataclysm models—Lunar cataclysm as a misconception (28 years later). *Meteorit. Planet. Sci.* 38, 579–593.

Hartmann, W.K. et al., 1981. Chronology of planetary volcanism by comparative studies of planetary cratering. In: *Basaltic Volcanism Study Project* (Ed.), *Basaltic Volcanism on the Terrestrial Planets*. Pergamon Press, New York, pp. 1049–1127.

Hiesinger, H., Jaumann, R., Neukum, G., Head III, J.W., 2000. Ages of mare basalts on the lunar nearside. *J. Geophys. Res.* 105, 29239–29275.

Hiesinger, H., Head, J.W., Wolf, U., Jaumann, R., Neukum, G., 2010. Ages and stratigraphy of lunar mare basalts in Mare Frigoris and other nearside maria based on crater size–frequency distribution measurements. *J. Geophys. Res.* 115, E03003. <http://dx.doi.org/10.1029/2009je003380>.

Hiesinger, H. et al., 2012. How old are young lunar craters? *J. Geophys. Res.* 117, E00H10. <http://dx.doi.org/10.1029/2011je003935>.

Holsapple, K.A., Housen, K.R., 2007. A crater and its ejecta: An interpretation of Deep Impact. *Icarus* 187, 345–356.

Le Feuvre, M., Wicczorek, M.A., 2011. Nonuniform cratering of the Moon and a revised crater chronology of the inner Solar System. *Icarus* 214, 1–20.

Malhotra, R., Strom, R.G., 2011. Comment on “Constraints on the source of lunar cataclysm impactors” (Cuk et al., 2010, *Icarus* 207, 590–594). *Icarus* 216, 359–362.

Marchi, S., Mottola, S., Cremonese, G., Massironi, M., Martellato, E., 2009. A new chronology for the Moon and Mercury. *Astron. J.* 137, 4936–4948.

Marchi, S., Massironi, M., Cremonese, G., Martellato, E., Giacomini, L., Prockter, L., 2011. The effects of the target material properties and layering on the crater chronology: The case of Raditladi and Rachmaninoff basins on Mercury. *Planet. Space Sci.* 59, 1968–1980.

Marchi, S., Bottke, W.F., Kring, D.A., Morbidelli, A., 2012. The onset of the lunar cataclysm as recorded in its ancient crater populations. *Earth Planet. Sci. Lett.* 325–326, 27–38.

Marchi, S. et al., 2013. Small crater populations on Vesta. *Planet. Space Sci.* in press.

McEwen, A.S., Bierhaus, E.B., 2006. The importance of secondary cratering to age constraints on planetary surfaces. *Annu. Rev. Earth Planet. Sci.* 34, 535–567.

- McEwen, A.S., Moore, J.M., Shoemaker, E.M., 1997. The phanerozoic impact cratering rate: Evidence from the farside of the Moon. *J. Geophys. Res.* 102, 9231–9242.
- Melosh, H.J., 1989. *Impact Cratering: A Geologic Process*, Oxford Monographs on Geology and Geophysics. Oxford Univ. Press, New York.
- Morbidelli, A., Vokrouhlický, D., 2003. The Yarkovsky-driven origin of near-Earth asteroids. *Icarus* 163, 120–134.
- Morbidelli, A., Marchi, S., Bottke, W.F., Kring, D.A., 2012. A sawtooth-like timeline for the first billion years of lunar bombardment. *Earth Planet. Sci. Lett.* 355–356, 144–151.
- Nesvorný, D., Morbidelli, A., Vokrouhlický, D., Bottke, W.F., Brož, M., 2002. The Flora family: A case of the dynamically dispersed collisional swarm? *Icarus* 157, 155–172.
- Neukum, G., Ivanov, B.A., 1994. Crater size distributions and impact probabilities on Earth from lunar, terrestrial-planet, and asteroid cratering data. In: Gehrels, T., Matthews, M.S., Schumann, A. (Eds.), *Hazards Due to Comets and Asteroids*. Univ. Arizona Press, Tucson, pp. 359–416.
- Neukum, G., Ivanov, B.A., Hartmann, W.K., 2001. Cratering records in the inner Solar System in relation to the lunar reference system. *Space Sci. Rev.* 96, 55–86.
- Prockter, L.M. et al., 2010. Evidence for young volcanism on Mercury from the third MESSENGER flyby. *Science* 329, 668–671.
- Robinson, M. et al., 2010. Lunar Reconnaissance Orbiter Camera (LROC) instrument overview. *Space Sci. Rev.* 150, 81–124.
- Schmidt, R.M., Housen, K.R., 1987. Some recent advances in the scaling of impact and explosion cratering. In: *Hypervelocity Impact Proceedings of the 1986 Symposium*, pp. 543–560 (International Journal of Impact Engineering).
- Simonson, B.M., Glass, B.P., 2004. Spherule layers – Records of ancient impacts. *Annu. Rev. Earth Planet. Sci.* 32, 329–361.
- Soderblom, L.A., Lebofsky, L.A., 1972. Technique for rapid determination of relative ages of lunar areas from orbital photography. *J. Geophys. Res.* 77, 279–296.
- Spudis, P.D., Wilhelms, D.E., Robinson, M.S., 2011. The Sculptured Hills of the Taurus Highlands: Implications for the relative age of Serenitatis, basin chronologies and the cratering history of the Moon. *J. Geophys. Res.* 116, E00H03. <http://dx.doi.org/10.1029/2011je003903>.
- Stöffler, D., Ryder, G., 2001. Stratigraphy and isotope ages of lunar geologic units: Chronological standard for the inner Solar System. *Space Sci. Rev.* 96, 9–54.
- Stöffler, D., Ryder, G., Ivanov, B.A., Artemieva, N.A., Cintala, M.J., Grieve, R.A.F., 2006. Cratering history and lunar chronology. *Rev. Mineral. Geochem.* 60, 519–596.
- Strom, R.G., Malhotra, R., Ito, T., Yoshida, F., Kring, D.A., 2005. The origin of planetary impactors in the inner Solar System. *Science* 309, 1847–1850.
- Wilhelms, D.E., 1987. *The Geologic History of the Moon*, U.S. Geol. Surv. Prof. Paper 1348. U.S. Geol. Surv., Washington, DC.
- Wünnemann, K., Marchi, S., Nowka, D., Michel, P., 2012. The effect of target properties on impact crater scaling and the lunar crater chronology. Presented at the 43rd Lunar Planet. Sci. Conf., Abst. #1805.